

Qualitative and Quantitative Assessment of the SET HASDM Database

Richard J. Licata^{1*}, Piyush M. Mehta¹, W. Kent Tobiska², Bruce R. Bowman², and Marcin D. Pilinski³

¹Department of Mechanical and Aerospace Engineering, West Virginia University, Morgantown, West Virginia, USA.

²Space Environment Technologies, Pacific Palisades, California, USA.

³Freestream, Boulder, Colorado, USA.

Key Points:

- Principal Component Analysis of HASDM and JB2008 Database covering almost two solar cycles.
- Dominant modes of variation are identified and compared.
- Statistical comparison with CHAMP and GRACE observations.

*1306 Evansdale Drive, Morgantown, West Virginia 26506-6106.

Corresponding author: Richard J. Licata, rjlicata@mix.wvu.edu

Abstract

The High Accuracy Satellite Drag Model (HASDM) is the operational thermospheric density model used by the US Space Force (USSF) Combined Space Operations Center (CSpOC). By using real-time data assimilation, HASDM can provide density estimates with increased accuracy over empirical models. With historical HASDM density data being released publicly for the first time, we can analyze the data to identify dominant modes of variations in the upper atmosphere. As HASDM is a close relative to the Jacchia-Bowman 2008 Empirical Thermospheric Density Model (JB2008), we look at time-matched density data to better understand the models' characteristics. This model comparison is conducted through the use of Principal Component Analysis (PCA). We then compare both datasets to the CHALLENGING Minisatellite Payload (CHAMP) and Gravity Recovery and Climate Experiment (GRACE) accelerometer-derived density estimates. By looking at the principal components and PCA scores from the two models, we confirm the increased complexity of the HASDM dataset while the CHAMP and GRACE comparisons show that HASDM more closely matches the accelerometer-derived densities with mean absolute differences of 23.81% and 30.84% compared to CHAMP and GRACE-A, respectively.

1 Introduction

Over the past seven decades, the scientific community has developed and advanced thermospheric density models. A significant subset of these models are empirical. Empirical models use long-term trends from measurements over an array of instruments to fit parametric equations that describe the system. Even within this subset, there are multiple families/series of models that use different types of measurements and have evolved over decades. Three of these series, discussed by Emmert (2015), are the MSIS (Picone *et al.* 2002), DTM (Bruinsma, Sean 2015), and Jacchia series (Bowman *et al.* 2008).

Mass Spectrometer Incoherent Scatter Radar (MSIS) models typically used mass spectrometer and incoherent scatter radar measurements but have evolved and now incorporate additional data (e.g. accelerometer-derived density estimates). The Drag Temperature Model (DTM) series used orbit-derived density data but more recently incorporates accelerometer-derived density and mass spectrometer data. The Jacchia series of models

43 (e.g. Jacchia-70 and JB2008) strictly use both orbit- and accelerometer-derived density
44 estimates.

45 The most recent in the Jacchia series is the JB2008 density model. JB2008 was an
46 improvement to its predecessors and incorporated new solar and geomagnetic indices to
47 drive the model. It uses the F_{10} , S_{10} , M_{10} , and Y_{10} indices and proxies to model variations
48 caused by solar heating. In addition to a_p , JB2008 utilizes Dst to better model density
49 during geomagnetic storms.

50 The thermosphere is a dynamic, highly-driven system impacted by external forces
51 (e.g. space weather events) and internal dynamics. Solar irradiance is a major source
52 of variation, providing the baseline average density (*Qian and Solomon 2011*). This pro-
53 cess is well-represented by solar indices, particularly at low latitudes (*Vickers et al. 2014*).
54 However, these indices are not adequate in characterizing the thermosphere during solar
55 minimum (*Bowman et al. 2008*), when composition changes and other processes become
56 more relevant (*Mehta et al. 2019*). During events like solar flares or coronal mass ejec-
57 tions (CMEs), mass and energy from the Sun interact with the magnetosphere causing
58 Joule heating and auroral particle precipitation into the thermosphere (*Fedrizzi et al. 2012*;
59 *Deng et al. 2013*). This causes sudden and often large changes in mass density. Due to a
60 lack of pre-storm conditioning and inability to model traveling atmospheric disturbances,
61 empirical models frequently under-perform during these events (*Bruinsma et al. 2021*).

62 The challenge of accurately modeling thermospheric mass density over a multitude
63 of conditions has severe repercussions in the context of orbit determination and Space Sit-
64 uational Awareness (SSA). Operators rely on these density models for decision making in
65 regards to collision avoidance operations, where inaccuracies and uncertainties can have
66 dire consequences. Insufficient knowledge of future satellite position can result in a col-
67 lision between two objects. A potential collision would drastically increase the number
68 of objects in a given orbital regime, increasing the probability of future collisions. This
69 could result in a cascade, known as Kessler Syndrome (*Kessler and Cour-Palais 1978*),
70 which could make certain orbital regimes inaccessible. In an effort to avoid this, we look
71 to improve our modeling and forecasting capabilities. A significant improvement in model
72 accuracy came from the implementation of real-time data assimilation, notably utilized by
73 HASDM.

74 HASDM was developed by Storz et al. (2005) and is an assimilative extension of
75 the Jacchia 1970 upper atmosphere density model (*Jacchia 1970*). HASDM employs Dy-
76 namic Calibration of Atmosphere (DCA) which uses calibration satellite observations
77 to make corrections to its background empirical density model. This assimilation tech-
78 nique was introduced as an application for HASDM by Casili and Barker (2002), but was
79 expanded later to estimate 13 global density correction parameters (*Storz et al. 2005*).
80 HASDM is not available for public use, but the global density outputs from the model
81 were released to the public for the first time by Tobiska et al. (2021). It is called the SET
82 HASDM density database. This database contains three-dimensional density grid from the
83 start of 2000 to the end of 2019 at a three-hour cadence.

84 In this work, we will leverage Principal Component Analysis (PCA) in order to
85 study the most dominant sources of variance within the HASDM dataset and a spatiotemporally-
86 matched JB2008 dataset. The resulting principal components and PCA scores give insight
87 into the processes that drive the variance within the models. This methodology has been
88 used to analyze thermospheric density datasets previously and is often used in the devel-
89 opment of reduced-order models (*Mehta and Linares 2017; Mehta et al. 2018; Gondelach*
90 *and Linares 2020*). For this paper, the use of PCA is restricted to scientific investigation.

91 The availability of accelerometer-derived density estimates has been advantageous
92 for model development and assessment. Over the lifetime of satellites with on board ac-
93 celerometers (e.g. CHAMP and GRACE), we accumulate measurements over a plethora
94 of altitudes and space weather conditions (*Luhr et al. 2002; Bettadpur 2012*). Researchers
95 have used these measurements to derive density estimates by removing accelerations from
96 other sources (*Sutton 2008; Doornbos 2012; Mehta et al. 2017*). We use the estimates
97 from (*Mehta et al. 2017*) for comparison with the HASDM and JB2008 models.

98 The paper is organized as follows, we start by detailing the HASDM and JB2008
99 models. Then, we discuss the use of PCA as an investigatory tool followed by the results
100 of the analysis. After, we compare the HASDM and JB2008 densities to CHAMP and
101 GRACE density estimate over the entire availability of their measurements, with a focus
102 on storm-time and quiet conditions.

2 Model Background

The most recent Jacchia model, JB2008, achieved improved accuracy largely due to its incorporations of new solar and geomagnetic indices. These indices are used in temperature corrections, semiannual functions, and new Dst temperature equations. The model reduced non-storm density errors by $> 5\%$ and reduced storm-time density errors from Jacchia-70 by $> 60\%$, from NRLMSIS by $> 35\%$ and from JB2008 (with only a_p) by 16% (Bowman *et al.* 2008).

Using a similar background density model, HASDM is able to further reduce these errors. By building on the density correction work of Marcos *et al.* (1998) and Nazarenko *et al.* (1998), HASDM can provide dynamic global density corrections via 13 spherical harmonic coefficients through its DCA algorithm. HASDM also exploits a prediction filter for its DCA corrections. Through this filter, the model adjusts an extrapolated time series of 27 days (one solar rotation) for the correction coefficients using wavelet and Fourier analysis (Storz *et al.* 2005). For satellite trajectory estimation, HASDM uses a technique, called segmented solution for ballistic coefficient (SSB), that enables the estimated ballistic coefficient to deviate over the fitting period.

2.1 Model Drivers

The most common solar proxy used in density modeling is $F_{10.7}$, referred to in this paper as F_{10} . Originally identified and measured by Covington (1948), F_{10} serves as a proxy for solar extreme ultraviolet (EUV) emissions which deposit energy into the thermosphere. The 10.7 in the subscript refers to the 10.7 cm wavelength of the solar radio flux being measured. While this does not directly interact with Earth's atmosphere, it has been shown to be a reliable proxy for thermospheric heating (Tobiska *et al.* 2008a). F_{10} is measured in solar flux units ($10^{-22} \text{W m}^{-2} \text{Hz}^{-1}$) indicated as *sfu*.

The S_{10} index characterizes the integrated 26-32 nm solar EUV emission. This index is influenced by temperatures in the chromosphere and solar corona (Tobiska *et al.* 2008a). These emissions penetrate into the middle thermosphere and are absorbed by atomic oxygen (Tobiska *et al.* 2008b). While the emissions that S_{10} represents have no relationship to the 10.7 cm wavelength, they are normalized and converted to *sfu* through linear regression. Similar fits are done for M_{10} and Y_{10} to convert to uniform units.

133 M_{10} is a proxy representative of far ultraviolet (FUV) photospheric 160 nm Schumann-
 134 Runge Continuum emissions. The proxy corresponds to processes in the lower thermo-
 135 sphere and is consistent with molecular oxygen dissociation (*Tobiska et al. 2008b*). The
 136 final solar driver for JB2008 is Y_{10} , which is a composite index. This hybrid represents X-
 137 ray emissions in the 0.1-0.8 nm range and H Lyman- α 121 nm emissions. During solar
 138 maximum, the X-ray emissions are more heavily weighted, and the opposite is true for so-
 139 lar minimum. For each of these four solar drivers, 81-day centered averages are generated
 140 and used for prediction in JB2008.

141 The first of the two geomagnetic drivers for JB2008 is the geomagnetic planetary
 142 amplitude, a_p . a_p is the linear equivalent of the geomagnetic planetary index, K_p , which
 143 has a quasi-logarithmic scale (*McClain and Vallado 2001*). It has a 3-hour cadence and is
 144 often used in density models. However, using Dst during geomagnetic storms results in
 145 increased accuracy over a_p for density modeling (*Bowman et al. 2008*). The Dst index is
 146 largely driven by the strength of the ring current in the inner magnetosphere. This makes
 147 it an ideal indicator of ring current strength and therefore geomagnetic storms (*Ganushk-*
 148 *ina et al. 2017*).

149 For operational use of HASDM, forecasts of these drivers are required. Space Envi-
 150 ronment Technologies (SET) provides the driver forecasts using multiple algorithms/sources.
 151 The solar drivers are forecasted using the *SOLAR200* algorithm (*Tobiska et al. 2000*). a_p
 152 forecasts come from the National Oceanic and Atmospheric Administration (NOAA) Space
 153 Weather Prediction Center (SWPC) forecasters, and Dst forecasts are produced by the
 154 *Anemilos* algorithm (*Tobiska et al. 2013*). Error statistics of historical forecasts for all
 155 six drivers were presented as a community benchmark by Licata et al. (2020).

156 In addition to these space weather drivers, the models use temporal inputs (e.g. uni-
 157 versal time (UT) and day of year). To model/correlate seasonal and annual trends, we gen-
 158 erated sinusoidal inputs based on the day of year. The first two are sine and cosine func-
 159 tions with periods of six months. This is used to test correlations with semiannual trends.
 160 The last two are sine and cosine functions with periods of one year to correlate with an-
 161 nual trends. We did not include any functions of UT, because it is difficult to find linear
 162 correlations with these short period fluctuations, particularly when the cadence of the data
 163 is only 1/8 of the function's period.

3 Principal Component Analysis

The spatial resolution of these models are 15° longitude, 10° latitude, and 25 km altitude spanning from 175-825 km. This results in 12,312 grid points for every three hours between the start of 2000 to the end of 2019. Principal Component Analysis is a dimensionality reduction technique that translates the dataset using linear functions to maximize variability and preserve information. The resulting information's dimensions are ordered from most-to-least contribution to the system's variance. Therefore, you can truncate the data at the desired point and only sacrifice a nominal amount of information (*Jolliffe and Cadima* 2016). This compaction forces important information from the dataset to be represented in fewer dimensions, simplifying the analysis.

In previous work, Mehta and Linares (2017) developed a methodology for reduced order modeling where PCA was used to reduce the dimensionality of MSIS densities. This allowed the authors to analyze the dominant sources of variance. We apply that same methodology (PCA implementation) to identify principal components for both the HASDM and JB2008 datasets. The steps to achieve this will be described, but the original work of (2017) provides a thorough description of the process. This methodology was used on a TIE-GCM dataset to create a linear dynamic reduced order model (*Mehta et al.* 2018).

Initially, the spatial dimensions are flattened to make the spatiotemporal dataset two-dimensional. Then a common logarithm of the density values is taken in order to reduce the variance of the dataset from five orders of magnitude to less than one. Next, we subtract the mean values for each cell to center the data. Finally, we perform a singular value decomposition using the *svds* function in *MATLAB* to obtain the \mathbf{U} , $\mathbf{\Sigma}$, and \mathbf{V} matrices. The normalized and centered density data is denoted by \mathbf{M} . Equation 1 shows the relationship between these four matrices and the basis of PCA.

$$\mathbf{M} = \mathbf{U}\mathbf{\Sigma}\mathbf{V}^T \quad (1)$$

The \mathbf{U} matrix is the left unitary matrix, and it is made of orthogonal vectors that represent the principal components. $\mathbf{\Sigma}$ is a diagonal matrix consisting of the squares of the eigenvalues that correspond to the vectors in \mathbf{U} . We can extract temporal coefficients (shown in Equation 2) by performing matrix multiplication between two of the components in Equation 1.

$$\mathbf{c}(\mathbf{t}) = \mathbf{\Sigma}\mathbf{V}^T \quad (2)$$

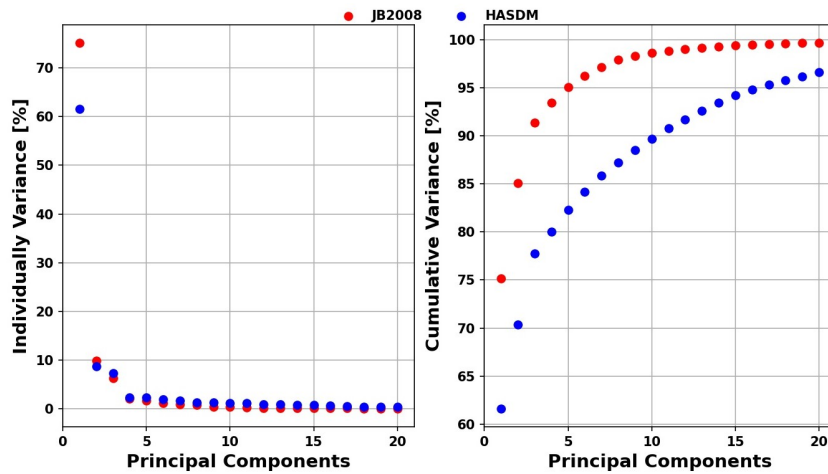
193 Using Σ , the energy/variance contribution of each principal component can be acquired as
 194 detailed in (Mehta and Linares 2017).

195 4 PCA Results

196 We begin by perform PCA on the entire dataset (2000-2020) to get insight into the
 197 general density formulations. Then, we look into specific conditions, such as solar maxi-
 198 mum and solar minimum, where different processes drive the global density variations.

199 4.1 2000-2020 Analysis

200 Figure 1 shows both the individual and cumulative variance captured by the first 20
 201 principal components (PCs). In the left subplot, it becomes clear that the contribution of
 202 the first PC for both models is significant, capturing over 60% of the system's total vari-
 203 ance. More importantly, the first PC for JB2008 captures over 10% more variance than it
 204 does for HASDM. There is also more variance captured by the second PC for JB2008, but
 205 beyond that, the individual variance captured is marginally greater for HASDM. This is
 206 due to the $\sim 75\%$ captured in the first PC for JB2008.

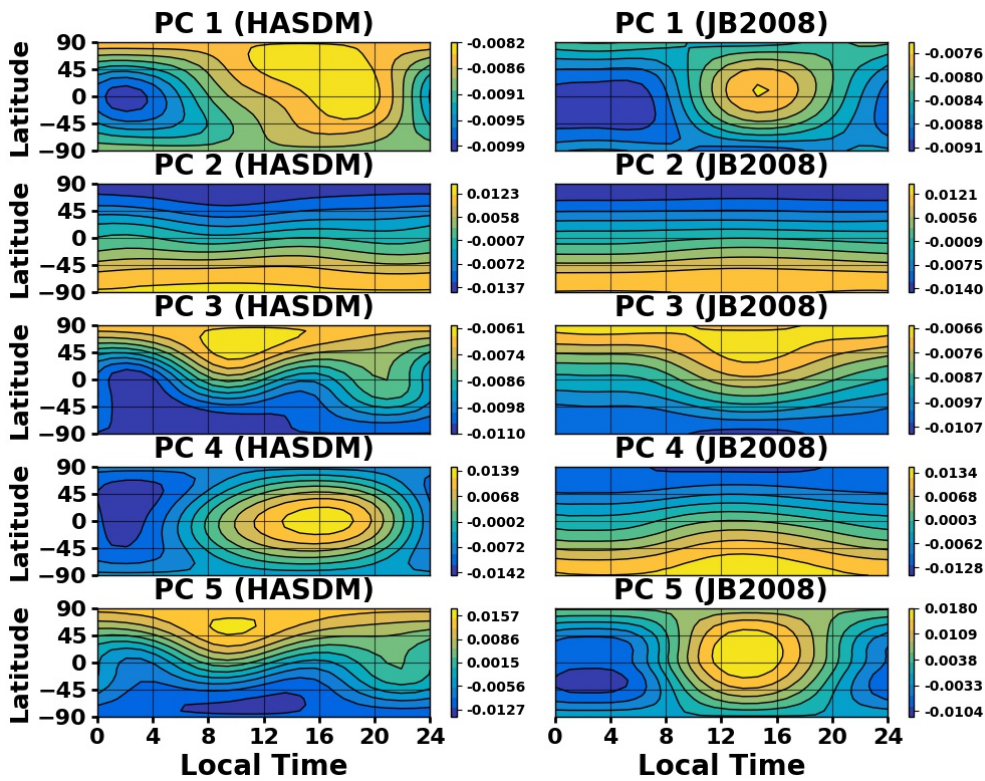


207 **Figure 1.** Individual (left) and cumulative (right) variance captured by the first 20 principal components
 208 for the two density datasets.

209 The cumulative variance is shown in the right subplot. It is abundantly clear that
 210 the variance captured by JB2008 is more substantial than by HASDM. Since JB2008 is an
 211 empirical model, there are well-defined relationships between the various drivers and the

212 overall system. Therefore, PCA is able to capture those processes in fewer PCs. HASDM,
 213 being an assimilative model, produces densities that account for an increased number of
 214 processes, making its structure more complex and more difficult to be captured by PCA.

215 Figures 2, 3, and 4 display the first five principal components (from U) for both
 216 models at 400 km, the first ten PCA scores (commonly referred to as temporal coeffi-
 217 cients), and the results from a Pearson's correlation coefficient analysis (*Schober et al.*
 218 2018) between the scores and drivers, respectively.



219 **Figure 2.** First five principal components for HASDM (left) and JB2008 (right) at 400 km.

225 The first PC for both models represents solar heating. There is peak around 14 hours
 226 local time and a minimum at 2 hours. Looking at this in relation to Figure 1, we can de-
 227 duce that the effect of solar heating contributes significantly more to JB2008 than it does
 228 for HASDM. From Figure 4, the first coefficient is highly correlated to F_{10} and the other
 229 solar indices; there is a 90% or greater correlation to all four solar indices/proxies and
 230 their centered averages. This explains the larger magnitude at solar maximum around 2001
 231 compared to around 2013. What also stands out is the not insignificant correlation to the

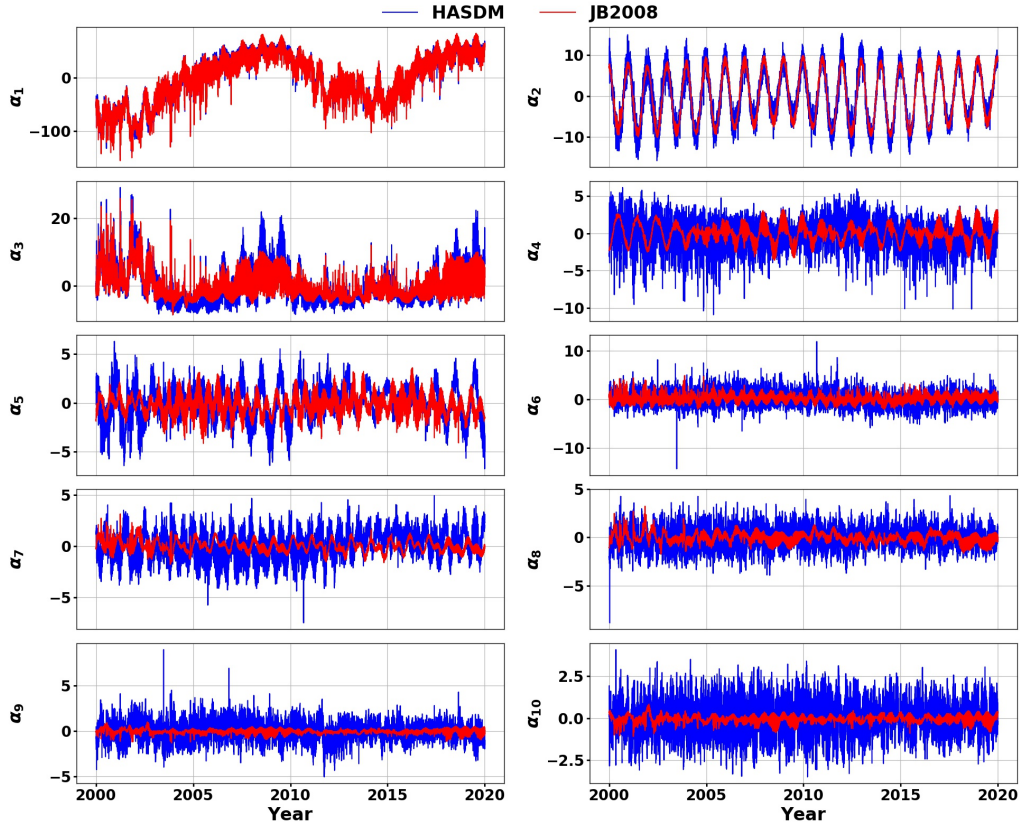


Figure 3. PCA scores/coefficients for both HASDM and JB2008 across two solar cycles.

geomagnetic indices. There are large spikes that coincide with events such as the Hal-
loween storm of 2003 and the St. Patrick's day storm of 2017.

The second PC likely represents annual variations. It shows how the density varies
fairly linearly with respect to latitude. Based on the day of year, this PC can change in
intensity and orientation. This is caused by the sinusoidal trend of α_2 with a period of
 ~ 365 days. The signs of the PCs and scores are important as they are multiplied for their
contribution.

The third PC is representing the same process(es) between the models. It is impor-
tant to note that PCA does not guarantee that a each PC corresponds to a single process.
Based on the first two, there is an evident dominant process representing it, but this is not
always the case. The third coefficient is the most complex of the first three. During solar
maximum, the trends seem to mimic coefficient 1, but its magnitude increases again dur-

HASDM(2000 – 2020)

	α_1	α_2	α_3	α_4	α_5	α_6	α_7	α_8	α_9	α_{10}
F_{10}	-0.91	-0.04	0.20	0.15	-0.02	0.01	0.03	-0.00	0.04	0.00
F_{81c}	-0.94	-0.04	0.16	0.15	-0.00	0.02	0.02	-0.01	0.02	-0.01
S_{10}	-0.96	-0.09	0.07	0.17	0.01	0.02	0.04	0.00	0.02	0.00
S_{81c}	-0.95	-0.09	0.04	0.16	0.02	0.03	0.03	-0.00	0.01	-0.01
M_{10}	-0.94	-0.09	0.16	0.16	-0.00	0.00	0.06	-0.01	0.03	0.01
M_{81c}	-0.94	-0.09	0.12	0.14	0.01	0.01	0.06	-0.01	0.01	-0.01
Y_{10}	-0.94	-0.10	0.02	0.15	0.03	0.01	0.08	-0.02	-0.02	-0.00
Y_{81c}	-0.94	-0.10	0.00	0.14	0.04	0.01	0.07	-0.02	-0.02	-0.02
ap	-0.26	-0.04	0.00	-0.47	-0.04	0.08	0.05	-0.01	0.01	-0.03
Dst	0.34	-0.01	-0.01	0.51	0.06	0.15	0.10	0.01	-0.09	0.03
semi _{sin}	0.06	-0.01	0.01	0.04	0.01	0.09	-0.04	0.01	-0.01	-0.03
semi _{cos}	0.11	0.05	0.13	0.09	0.18	0.01	0.58	-0.06	0.05	-0.11
ann _{sin}	-0.04	-0.17	-0.03	-0.03	-0.06	0.00	-0.05	-0.09	0.00	-0.05
ann _{cos}	-0.14	0.94	-0.10	0.00	-0.14	0.00	-0.01	-0.02	0.01	0.00

JB2008(2000 – 2020)

	α_1	α_2	α_3	α_4	α_5	α_6	α_7	α_8	α_9	α_{10}
F_{10}	-0.90	-0.03	0.18	-0.01	-0.01	-0.19	-0.07	0.02	0.11	0.07
F_{81c}	-0.92	-0.04	0.13	-0.02	-0.02	-0.16	-0.03	-0.02	0.10	0.09
S_{10}	-0.95	-0.08	0.06	-0.01	0.01	-0.19	-0.02	0.01	0.06	0.05
S_{81c}	-0.94	-0.08	0.02	-0.01	0.02	-0.17	-0.00	-0.01	0.05	0.05
M_{10}	-0.93	-0.08	0.13	-0.01	-0.02	-0.18	-0.04	-0.01	0.08	0.07
M_{81c}	-0.93	-0.09	0.09	-0.02	-0.01	-0.15	-0.02	-0.04	0.07	0.08
Y_{10}	-0.93	-0.10	-0.00	-0.01	-0.03	-0.18	-0.06	0.00	0.04	0.03
Y_{81c}	-0.93	-0.10	-0.02	-0.01	-0.02	-0.15	-0.03	-0.02	0.04	0.04
ap	-0.25	-0.05	0.02	0.01	-0.18	0.31	0.06	0.01	-0.12	-0.14
Dst	0.35	-0.01	-0.08	0.01	0.21	-0.42	-0.07	-0.06	0.14	0.14
semi _{sin}	0.07	-0.00	-0.09	-0.10	-0.23	-0.49	0.57	-0.14	-0.01	-0.08
semi _{cos}	0.12	0.02	-0.03	-0.17	-0.69	-0.06	0.05	0.11	0.10	0.14
ann _{sin}	-0.06	-0.18	0.00	0.04	0.16	0.09	0.65	-0.33	0.00	0.07
ann _{cos}	-0.14	0.97	-0.07	0.02	0.03	0.01	0.12	-0.05	-0.03	0.05

221 **Figure 4.** Pearson correlation coefficients between all inputs and PCA scores for HASDM
 222 and JB2008 between 2000 and 2020. The sum of the absolute values for HASDM and JB2008
 223 are 16.95 and 20.70, respectively. The colors represent the correlation coefficients with blue
 224 being -1.0, white being 0.0, and red being 1.0.

244 ing solar minimum. This increase no longer seems to relate to the first coefficient. Based
 245 on the correlation values, it can be deduced that the third PC is mostly representative of
 246 solar activity in regards to the entire time period. The combination of processes captured
 247 by this principal component makes linear correlation analysis difficult, especially over this
 248 time span. Looking at shorter windows (see the next two subsections) uncovers different
 249 processes captured by α_3 , depending on the conditions.

250 In Supplementary Material SM1, the movement of the peak in α_3 provides insight to
 251 HASDM. At lower altitudes (250-450 km), the HASDM peak has a ~ 4 hour shift rela-
 252 tive to JB2008 which is seen in Figure 2. The JB2008 peak is located between 12 and 14
 253 hours local time while HASDM's are around 9 hours. Beyond 450 km, the peak in both
 254 models shifts to 2 hours local time and towards the equator. They exhibit similar trends
 255 up to 825 km which hints at the reliance on HASDM's background model when the sig-
 256 nal decreases at higher altitudes. We suspect that this represents the Winter helium bulge
 257 based on the local time of the peak (*Keating and Prior 1968; Reber and Hays 1973*).

258 The last two PCs shown in Figure 2 for the two models are flipped, meaning the
 259 fourth for HASDM has the same source as the fifth for JB2008 and vice versa. There is
 260 only a 2.25% difference between PCs 4 and 5 for HASDM which signifies that their re-
 261 spective contribution to the system's overall variance is similar. PC 4 for HASDM and
 262 5 for JB2008 seem to be further effects of solar heating, while the other two are similar
 263 to PC 3. α_4 for HASDM and α_5 for JB2008 both have some correlation to geomagnetic
 264 activity, while α_5 for JB2008 has moderately strong correlation to the semiannual cosine
 265 wave. In Figure 2, the difference between PCs 3 and 5 for HASDM and PCs 3 and 4 for
 266 JB2008 is the location of the peak present in either the northern or southern poles.

267 Note that in the caption, the absolute sum for both models is shown, and the value
 268 for JB2008 is over 20% larger than for HASDM. This is as expected due to the simplicity
 269 in the density formulation of an empirical model relative to an assimilative one. Beyond
 270 these discussed principal components and scores, there is not an abundance of informa-
 271 tion. These correlation coefficients were generated using the entire twenty year period.
 272 However, looking at the coefficient plots and correlations for a single year shows that there
 273 is more information that cannot be seen by looking at such a broad period.

274 4.2 Solar Maximum

275 Figure 5 shows the first ten PCA scores for both models during 2001 (solar maxi-
 276 mum), and Figure 6 contains the corresponding correlation coefficients.

282 The first coefficients for both models in Figure 5 are nearly identical, alluding to the
 283 similarities in how solar drivers impact the resulting density grids in both models. There
 284 is lower correlation between α_1 and the solar drivers relative to the twenty-year analysis.
 285 There is now increased correlation with the other drivers (e.g. geomagnetic and temporal).

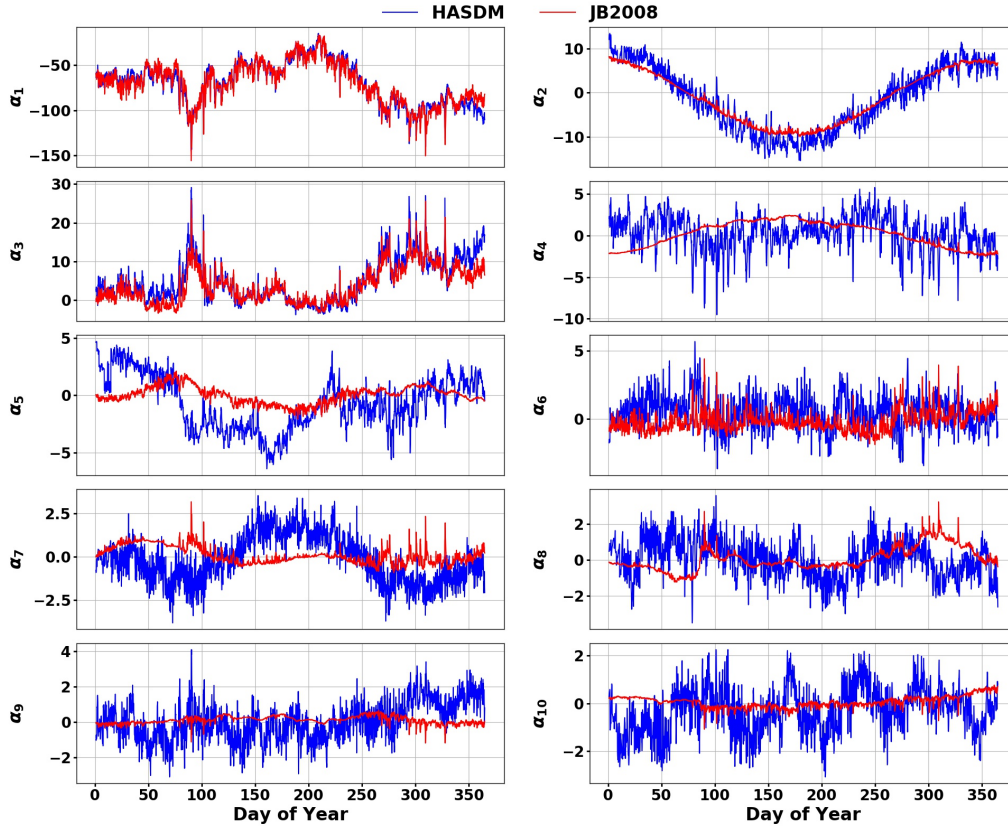


Figure 5. PCA coefficients for both HASDM and JB2008 for 2001.

277

286 The geomagnetic indices have more correlation during this year, because there is a larger
 287 portion of the time period with moderate or high geomagnetic activity compared to the
 288 complete period. There are also increases in correlation for the temporal drivers, but it is
 289 not entirely clear if that is coincidental with how solar heating varied over this particular
 290 year.

291 α_2 again shows a distinct annual trend, but there are some differences highlighted
 292 by the shortened time period. The variation for HASDM seems to contain additional pro-
 293 cesses, identified by the more complex structure within the mean annual trend. There is
 294 a strong correlation with the annual cosine wave, as was the case for the entire period.
 295 Similar to α_1 , there are moderate correlations with all of the solar drivers. This is again
 296 likely a byproduct of how the solar drivers varied over the year. This is reinforced by the
 297 correlation values for JB2008 combined with the near-perfect cosine wave seen in Figure
 298 5.

HASDM(2001)										
	α_1	α_2	α_3	α_4	α_5	α_6	α_7	α_8	α_9	α_{10}
F_{10}	-0.77	0.37	0.77	-0.17	0.01	-0.06	-0.48	-0.01	0.54	0.27
F_{81c}	-0.75	0.52	0.72	-0.18	0.18	-0.14	-0.59	-0.06	0.58	0.20
S_{10}	-0.86	0.48	0.86	-0.24	0.07	-0.08	-0.54	-0.01	0.61	0.24
S_{81c}	-0.77	0.63	0.73	-0.18	0.29	-0.12	-0.60	-0.07	0.60	0.14
M_{10}	-0.76	0.41	0.78	-0.20	0.05	-0.12	-0.41	-0.07	0.57	0.17
M_{81c}	-0.69	0.57	0.68	-0.16	0.26	-0.14	-0.49	-0.15	0.60	0.12
Y_{10}	-0.73	0.35	0.73	-0.14	-0.00	-0.02	-0.44	-0.01	0.51	0.30
Y_{81c}	-0.75	0.54	0.72	-0.17	0.21	-0.14	-0.60	-0.05	0.58	0.20
ap	-0.35	0.04	0.42	-0.54	-0.10	-0.04	-0.15	-0.02	0.14	0.10
Dst	0.56	-0.17	-0.57	0.64	0.10	0.30	0.44	-0.00	-0.33	-0.19
semi _{sin}	0.41	0.07	-0.41	0.34	0.41	0.15	0.19	0.09	-0.31	-0.06
semi _{cos}	0.40	-0.02	-0.31	0.09	0.16	-0.05	0.54	-0.35	-0.00	-0.29
ann _{sin}	0.21	-0.12	-0.26	-0.09	-0.05	0.13	0.06	0.26	-0.35	-0.21
ann _{cos}	-0.59	0.95	0.49	-0.08	0.74	0.03	-0.62	0.12	0.38	-0.11

JB2008(2001)										
	α_1	α_2	α_3	α_4	α_5	α_6	α_7	α_8	α_9	α_{10}
F_{10}	-0.74	0.43	0.74	-0.35	0.40	0.28	-0.15	0.66	0.06	0.32
F_{81c}	-0.72	0.61	0.71	-0.59	0.36	0.39	-0.30	0.70	-0.14	0.57
S_{10}	-0.83	0.55	0.83	-0.48	0.38	0.40	-0.08	0.72	-0.05	0.41
S_{81c}	-0.73	0.72	0.70	-0.70	0.35	0.41	-0.23	0.67	-0.24	0.66
M_{10}	-0.73	0.48	0.76	-0.44	0.23	0.34	-0.14	0.68	-0.02	0.40
M_{81c}	-0.65	0.65	0.67	-0.67	0.21	0.40	-0.31	0.67	-0.23	0.66
Y_{10}	-0.71	0.41	0.69	-0.33	0.40	0.26	-0.13	0.60	0.06	0.29
Y_{81c}	-0.72	0.62	0.70	-0.60	0.38	0.38	-0.27	0.68	-0.15	0.58
ap	-0.30	0.01	0.34	0.06	0.08	0.41	0.28	0.24	-0.23	-0.24
Dst	0.60	-0.19	-0.64	0.10	-0.21	-0.67	-0.35	-0.51	0.41	0.21
semi _{sin}	0.42	0.00	-0.51	-0.02	0.05	-0.41	0.47	-0.57	-0.03	0.03
semi _{cos}	0.41	-0.01	-0.32	-0.16	-0.70	-0.03	-0.09	-0.26	-0.29	0.24
ann _{sin}	0.23	-0.16	-0.37	0.22	0.09	-0.07	0.49	-0.54	-0.07	-0.29
ann _{cos}	-0.57	0.98	0.35	-0.96	0.51	0.22	0.38	0.21	-0.58	0.74

278 **Figure 6.** Pearson correlation coefficients between all inputs and PCA scores for HASDM and JB2008
 279 only during 2001 (solar maximum). The sum of the absolute values for HASDM and JB2008 are 45.82
 280 and 56.76, respectively. The colors represent the correlation coefficients with blue being -1.0, white being
 281 0.0, and red being 1.0.

299 The third coefficient is nearly a mirror image of the first coefficient for both HASDM
 300 and JB2008. This was suspected when looking at the coefficient plot for the entire period,
 301 but it did not show up in the correlation values from Figure 4. Clearly, α_3 contains mul-
 302 tiple processes that are difficult to observe from afar. The correlation values for α_3 with
 303 both models is almost exactly the opposite of the values for α_1 which reinforces the obser-
 304 vation.

305 α_4 is quite interesting as it is representing different processes between the models
 306 and more than one for HASDM. For JB2008 it is inversely correlated to an annual cosine
 307 wave with little influence from another source. However, α_4 for HASDM shows some re-
 308 lation to a semiannual trend with influence from geomagnetic storms, having large spikes
 309 that coincide with those in α_1 which is reaffirmed by the correlation coefficients.

310 The fifth coefficient for HASDM has quite a peculiar set of correlation values. Its
 311 most significant correlations are to a semiannual sine wave and an annual cosine wave.
 312 Looking at Figure 5, it visually appears noisy, because the spikes do not correspond to
 313 spikes in the other coefficients. However, there are likely other contributions not captured
 314 by these drivers. For JB2008, there are non-negligible correlations with the solar drivers
 315 and the temporal cosine inputs.

316 Other interesting findings for 2001 include HASDM's α_7 and α_9 along with JB2008's
 317 α_8 and α_{10} . HASDM's seventh coefficient visually shows a strong semiannual trend. When
 318 looking at Figure 6, there is more correlation to the annual trend and most of the solar in-
 319 dices. This is peculiar, because the qualitative study of the coefficient shows much more
 320 signal in relation to a semiannual variation. After consulting the correlation coefficients
 321 for HASDM's α_9 , the similarity to α_1 and α_3 becomes more clear. It seems to be largely
 322 influenced by solar heating but is less evident.

323 The eighth coefficient for JB2008 at first glance looks to have a semiannual quality,
 324 but after looking at the correlation values, its relationship to solar heating becomes more
 325 apparent. In fact, it looks like the third coefficient, only with a visually stronger signal.
 326 JB2008's α_{10} likely represents an annual cosine wave. However, it is difficult to see due to
 327 the y-axis bounds determined by the range of α_{10} for HASDM.

328 The most distinct difference between Figure 4 and 6 is the increase in the prevalence
 329 of color and therefore significant correlations. Nearly every coefficient for both models has
 330 at least one driver with 40% or greater correlation. Again, JB2008 has more cumulative
 331 correlation than HASDM, due to the increased processes in HASDM not modeled by the
 332 current set of drivers.

333

4.3 Solar Minimum

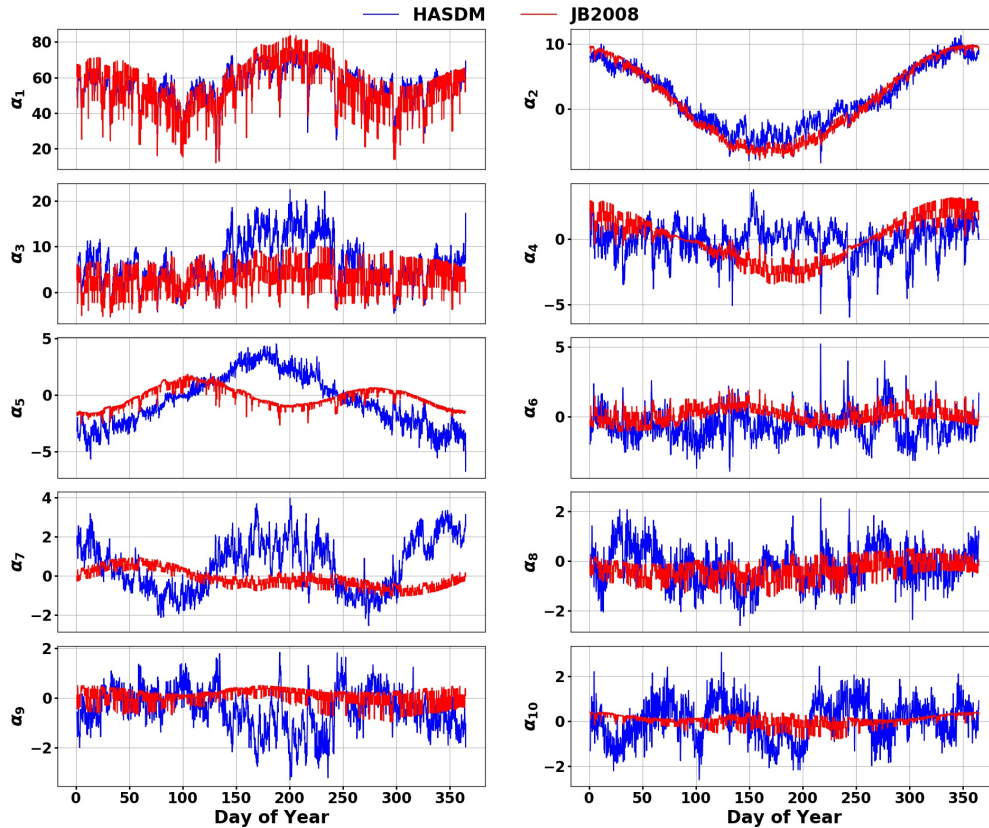
334

335

336

337

With the plethora of new information obtained by looking at the coefficients during a shorter period of solar maximum, it is important to see differences during solar minimum. Figure 7 shows the coefficients for both models during 2019, and Figure 8 contains the corresponding correlation coefficients.



338

Figure 7. PCA coefficients for both HASDM and JB2008 for 2019.

343

344

345

346

347

348

349

Visually, some coefficients show stark contrasts to 2001. Primarily, α_1 for both models represents a noisy semiannual cosine wave. The apparent noise is even peculiar; it seems to jump between a fixed range about the mean for most of the year. Another notable difference between the years for α_1 is the change in sign. For 2001, all values were negative and mostly larger in magnitude, but the 2019 values are all positive. The correlations for α_1 deviate from the previous two cases. There is no longer a strong correlation between α_1 and solar heating for either model. In fact, the correlation with geomagnetic

HASDM(2019)										
	α_1	α_2	α_3	α_4	α_5	α_6	α_7	α_8	α_9	α_{10}
F ₁₀	-0.43	0.21	-0.45	0.09	-0.31	-0.15	-0.11	0.05	0.33	-0.05
F _{81c}	-0.43	0.36	-0.51	0.06	-0.46	-0.11	-0.12	0.03	0.31	0.06
S ₁₀	-0.33	-0.25	-0.27	0.08	0.17	-0.14	-0.13	-0.14	0.28	-0.05
S _{81c}	-0.22	-0.34	-0.17	0.08	0.28	-0.08	-0.02	-0.28	0.13	0.06
M ₁₀	-0.17	-0.32	-0.08	0.12	0.27	-0.10	-0.02	-0.18	0.12	-0.02
M _{81c}	0.00	-0.59	0.11	0.05	0.58	-0.04	0.08	-0.39	-0.06	0.11
Y ₁₀	0.15	-0.28	0.24	0.16	0.34	-0.04	0.36	-0.20	-0.26	0.08
Y _{81c}	0.22	-0.36	0.32	0.13	0.44	0.01	0.39	-0.30	-0.31	0.06
ap	-0.45	-0.10	-0.36	-0.51	0.07	0.25	-0.15	0.12	0.26	-0.02
Dst	0.58	0.03	0.50	0.49	0.02	0.06	0.28	-0.13	-0.41	-0.07
semi _{sin}	0.22	0.03	0.19	-0.07	-0.04	0.05	-0.17	0.26	-0.04	-0.05
semi _{cos}	0.45	0.08	0.49	0.31	0.08	0.07	0.80	-0.01	-0.48	-0.31
ann _{sin}	-0.17	-0.19	-0.16	0.09	0.10	-0.10	-0.14	-0.09	0.19	-0.07
ann _{cos}	-0.37	0.95	-0.51	0.04	-0.95	-0.05	0.06	0.31	0.21	0.02

JB2008(2019)										
	α_1	α_2	α_3	α_4	α_5	α_6	α_7	α_8	α_9	α_{10}
F ₁₀	-0.37	0.23	-0.24	0.32	0.17	0.03	0.38	0.06	-0.09	0.31
F _{81c}	-0.43	0.37	-0.22	0.45	0.20	0.08	0.57	-0.09	-0.13	0.40
S ₁₀	-0.33	-0.21	-0.16	-0.07	0.37	0.31	0.02	0.08	0.09	0.14
S _{81c}	-0.33	-0.34	-0.02	-0.17	0.55	0.52	0.02	-0.16	0.12	0.08
M ₁₀	-0.16	-0.29	-0.02	-0.17	0.31	0.23	-0.17	0.06	0.05	-0.01
M _{81c}	-0.14	-0.60	0.14	-0.45	0.54	0.54	-0.36	-0.10	0.17	-0.16
Y ₁₀	0.09	-0.29	0.22	-0.23	0.08	0.27	-0.58	0.07	0.07	-0.06
Y _{81c}	0.11	-0.38	0.27	-0.31	0.12	0.37	-0.72	0.09	0.11	-0.12
ap	-0.30	-0.07	-0.37	-0.06	-0.05	0.28	0.16	0.27	0.17	0.04
Dst	0.42	0.02	0.48	-0.00	0.06	-0.33	-0.22	-0.39	-0.19	-0.13
semi _{sin}	0.35	0.01	-0.10	-0.13	-0.39	-0.59	0.55	-0.17	0.03	-0.20
semi _{cos}	0.54	0.04	0.11	-0.08	-0.76	-0.13	-0.06	-0.10	0.30	0.26
ann _{sin}	-0.17	-0.20	-0.18	-0.13	0.27	0.10	0.70	-0.39	0.16	0.10
ann _{cos}	-0.29	0.98	-0.15	0.94	-0.31	-0.20	0.20	0.29	-0.36	0.57

339 **Figure 8.** Pearson correlation coefficients between all inputs and PCA scores for HASDM and JB2008
 340 only during 2019 (solar minimum). The sum of the absolute values for HASDM and JB2008 are 30.02
 341 and 34.10, respectively. The colors represent the correlation coefficients with blue being -1.0, white being
 342 0.0, and red being 1.0.

350 activity is more pronounced than solar heating. The correlation with the semiannual co-
 351 sine wave is the strongest of the inputs for JB2008 and one of the strongest for HASDM.

352 During this solar minimum, there was very low solar activity and few active regions
 353 giving the usual 27-day signal a longer 3-4 month signal, so other processes begin to
 354 dominate. This explains why the PCA coefficients are drastically dissimilar to those of so-
 355 lar maximum, and why other drivers become more pronounced. Looking at the cumulative

356 correlation for the models, there is a substantial decrease from solar maximum; they are
 357 approximately 60% and 65% of the 2001 values for HASDM and JB2008, respectively.

358 α_2 for both models is again a clear annual cosine wave. In comparison to 2001, the
 359 values and variance for the two models are more aligned. There is a strong positive corre-
 360 lation to the annual cosine wave, as was the case for the other two periods.

361 For both HASDM and JB2008, α_3 is difficult to visually discern. There are no sig-
 362 nificant long-term variations for JB2008. The only drivers with correlations greater than
 363 30% are the two geomagnetic indices. The general appearance of α_3 is similar for HASDM
 364 but it has a relatively sharp increase about 1/3 through the year, and a drop around 2/3
 365 through the year. HASDM has similar correlation values for the geomagnetic indices but
 366 also has noteworthy correlations to the temporal drivers and to F_{10} .

367 α_4 for HASDM has no apparent long-term trend (similar to JB2008's α_3), but it is
 368 moderately correlated to the geomagnetic drivers. For JB2008, there is a strong positive
 369 correlation to the annual cosine wave, which can be seen in the coefficient's trend. α_5 has
 370 temporal trends for both models, but it is semiannual for JB2008 and annual for HASDM.
 371 Both show a strong signal.

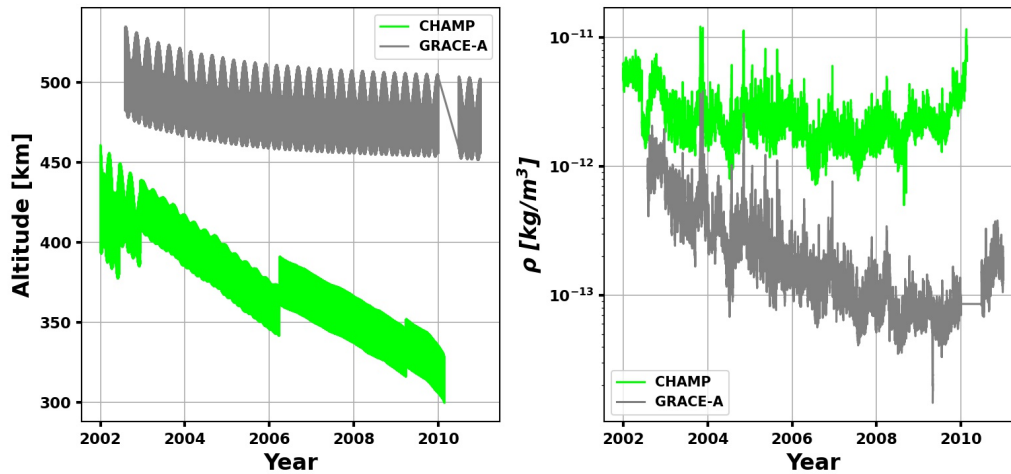
372 All the higher order coefficients are either temporal variations or indistinct, with the
 373 exception of α_7 for JB2008. It appears to have a semiannual component, but the baseline
 374 seems to decrease linearly. Oddly, α_7 shows to be more strongly correlated to the annual
 375 sine wave than the semiannual sine wave. This coefficient also has a 72% negative corre-
 376 lation to Y_{81c} . However, the variation's source is not definitive.

377 The largest correlation to any solar driver for HASDM is the correlation to M_{81c}
 378 in α_2 and α_5 , but that is likely a consequence of those two coefficients being highly cor-
 379 related to the annual cosine wave. The only other notable connection for HASDM is the
 380 strong positive correlation to the semiannual cosine wave in α_7 . In fact, the three strongest
 381 correlations for HASDM are to temporal drivers.

382 **5 CHAMP & GRACE Density Estimates**

383 The CHAMP and GRACE datasets used in this study originate from Mehta et al.
 384 (2017). Both satellites have near polar orbits, covering nearly all latitudes, and over their
 385 respective lifetimes, CHAMP and GRACE datasets cover altitudes ranging from 300-535

386 km. This, in conjunction with the date range covered by the satellites, makes their density
 387 estimates invaluable for model comparison. Figure 9 shows altitudes each dataset cov-
 388 ers along with orbit-averaged densities over their mission spans. This study only included
 389 GRACE-A data due to similarities between the twin satellites' orbits.



390 **Figure 9.** Altitude (left) and orbit-averaged densities (right) for CHAMP and GRACE-A.

391 There is minimal overlap between the altitudes of the two satellites, resulting in the
 392 lower densities encountered by GRACE-A in the right panel. The orbit-averaged densities
 393 were computed using a centered window with a span of 90 minutes, approximately one
 394 orbit.

395 Both the CHAMP and GRACE-A datasets contain files for every day containing in-
 396 formation such as GPS time, solar local time (SLT), latitude, altitude and density. CHAMP
 397 has measurements every 10 seconds, while GRACE-A provides measurements every 5 sec-
 398 onds. In order to compare the satellite density estimates to the two models, we implement
 399 a trilinear interpolation algorithm using the global density grids from the models. Since
 400 the temporal resolution of the model densities are only every three hours, we maintain
 401 the same density grids over each three-hour period. The authors appended the existing
 402 CHAMP and GRACE density data of (Mehta *et al.* 2017) with the HASDM and JB2008
 403 densities and have made them publicly available to the community (see Data Statement).

6 Model-Satellite Density Comparison

Figure 10 shows histograms of the \log_{10} orbit-averaged densities for both satellites and models. HASDM and JB2008 overpredict relative to CHAMP and GRACE-A. However, the HASDM distributions have a marginally smaller bias for both satellites. The shape of the HASDM distributions more closely matches the high fidelity CHAMP and GRACE-A estimates with the smaller peaks being present on the right side. The JB2008 has similar distributions to both satellites but appears more generalized.

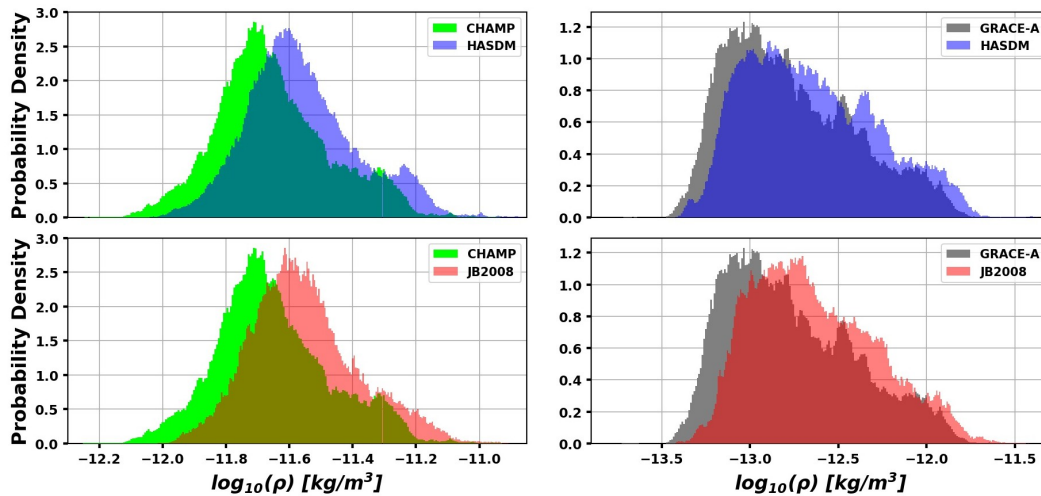


Figure 10. Histograms for CHAMP (left) and GRACE-A (right) orbits and corresponding densities from HASDM (top) and JB2008 (bottom). Values are centered averages with a window of 90 minutes, approximately one orbit.

Having spatiotemporally matched model densities to every measurement, mean absolute differences were computed for both the orbit and orbit-averaged densities. The results are shown in Table 1, broken down by year.

HASDM densities more closely match both CHAMP and GRACE-A estimates overall. However, there are years for both satellites where JB2008 predicts densities closer to the satellite estimates. The general trend is increased similarities to the satellite densities towards solar maximum, which decreases towards solar minimum. The models have lower percent differences when looking at orbit-averaged values, because they are tracking general density trends much better than the short period disturbances. The decrease in the density differences range from 3 – 13% and 4 – 15% for HASDM and JB2008, respec-

417 **Table 1.** Mean absolute percent difference error statistics for both models and satellites.

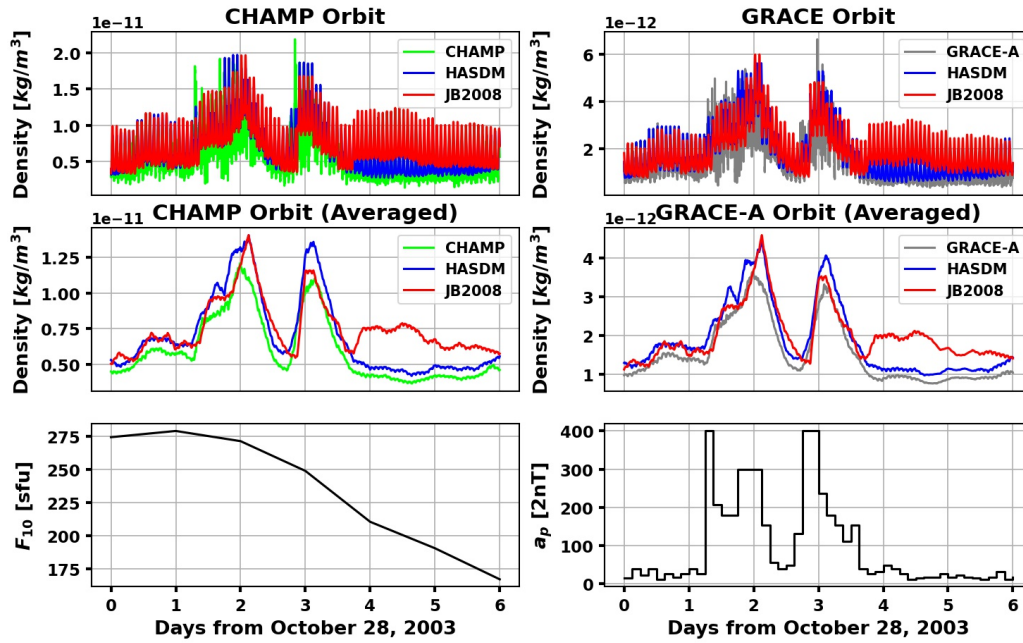
418 "OA" denotes orbit-averaged.

	CHAMP		CHAMP (OA)		GRACE-A		GRACE-A (OA)	
Year	HASDM	JB2008	HASDM	JB2008	HASDM	JB2008	HASDM	JB2008
All	29.35%	33.96%	23.81%	27.63%	41.80%	50.52%	30.84%	39.75%
2002	22.10%	24.31%	19.31%	20.37%	27.70%	29.66%	23.03%	24.50%
2003	23.04%	23.26%	19.48%	18.58%	35.91%	36.97%	29.64%	28.81%
2004	25.23%	22.88%	21.57%	17.88%	41.05%	38.04%	34.22%	30.45%
2005	28.24%	33.29%	23.92%	28.52%	45.06%	57.95%	37.02%	50.45%
2006	29.72%	39.85%	24.47%	34.38%	36.90%	53.41%	30.67%	48.31%
2007	31.33%	37.99%	25.29%	31.77%	48.20%	63.89%	30.47%	45.20%
2008	41.31%	50.44%	28.07%	35.59%	40.65%	52.55%	24.67%	38.43%
2009	33.66%	41.80%	27.93%	35.62%	49.11%	63.35%	29.06%	45.25%
2010	32.33%	24.52%	28.05%	20.49%	44.69%	41.75%	37.44%	34.05%

426 tively when comparing the orbit to orbit-averaged differences for CHAMP. For GRACE-
427 A, the differences are more pronounced, being 5 – 20% for HASDM and 5 – 19% for
428 JB2008. Considering the similarity in orbit inclination, this disagreement between the or-
429 bit and orbit-averaged differences is likely attributed to the altitude. To more closely ex-
430 amine the densities, we look at both active and quiet six-day periods (Figures 11 and 12
431 respectively). Figure 11 shows densities along CHAMP and GRACE-A orbits during the
432 2003 Halloween storm.

435 Looking at the storm time drivers, F_{10} starts off with substantial magnitude before
436 decaying during the geomagnetic storms. a_p peaks at the maximum possible value of 400
437 twice during this period; it happening even once is an extremely rare occurrence. Outside
438 of these storms, there is little geomagnetic activity. For the quiet period, F_{10} remains at
439 solar minimum levels, and stays between 69 and 70 *sfu*. Concurrently, a_p varies contin-
440 uously but never exceeds 12 ($K_p = 3$ -). The densities spike on two occasions, coinciding
441 with the two geomagnetic storms. When a_p initially reaches 400, the density responds to
442 about half the magnitude increase of the first peak. a_p then drops before maintaining 300
443 $2nT$ for a few hours; this is immediately before the density reaches its maximum value for
444 this storm as there is a delayed density response.

445 There is a quicker overall response to the second storm, when a_p maintains its max-
446 imum value for a longer duration. Pre-storm conditioning could also cause the more abrupt

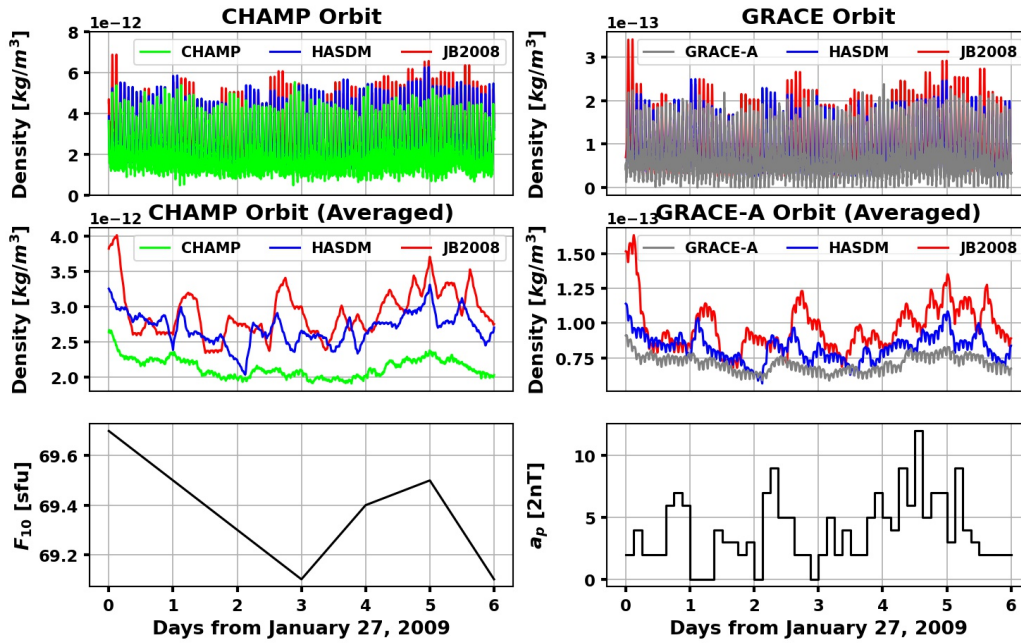


433 **Figure 11.** Densities from CHAMP, GRACE-A, HASDM, and JB2008 following a storm period
 434 in 2003. Center panels are orbit-averaged densities, and bottom panels show F_{10} and a_p .

447 density response. These trends are true for both satellite orbits. HASDM and JB2008 both
 448 have similar small biases before the storm, and HASDM over-predicts density relative to
 449 the satellites and JB2008.

450 However, the density recovery post-storm is modeled significantly closer to the satel-
 451 lite by HASDM than JB2008. This divergence may be caused by the NO production dur-
 452 ing the storm, a known cooling mechanism. This flows meridionally towards the equator
 453 in the days after the storm and is captured by HASDM but not modeled in JB2008. The
 454 mean differences for orbit-averaged densities with respect to CHAMP are 16.27% and
 455 34.33% for HASDM and JB2008, respectively. Relative to GRACE-A, the mean differ-
 456 ences are 23.09% and 46.58% for HASDM and JB2008, respectively. In Figure 12, the
 457 same information is presented for a quiet period in 2009.

460 In the orbit density plots, both models follow the oscillations well but have posi-
 461 tive biases. Again, HASDM is tracking the satellite densities more closely than JB2008.
 462 This is confirmed in the orbit-averaged plots with HASDM being discernibly closer to
 463 the satellite densities. JB2008 predicts density closer to HASDM for CHAMP (lower al-



458 **Figure 12.** Densities from CHAMP, GRACE-A, HASDM, and JB2008 during a quiet period
 459 in 2009. Center panels are orbit-averaged densities, and bottom panels show F_{10} and a_p .

464 titude) than for GRACE-A. Referring back to Figure 9, the difference in average altitude
 465 for the satellites in 2009 is approximately 150 km. This explains the order of magni-
 466 tude difference in densities and shows that HASDM more closely matches satellite esti-
 467 mates at higher altitudes. The mean differences for orbit-averaged densities with respect
 468 to CHAMP are 26.34% and 37.07% for HASDM and JB2008, respectively. Regarding to
 469 GRACE-A, the mean differences are 15.81% and 36.28% for HASDM and JB2008, re-
 470 spectively.

471 There are considerable peaks in the JB2008 densities, seen in all four panels. It is
 472 more pronounced in the orbit-averaged density plots, particularly for the GRACE-A orbit.
 473 These seem to be a response to the geomagnetic activity (seen in the bottom-right panel).
 474 All JB2008 density peaks lag a_p spikes by about 12 hours and deviate from HASDM and
 475 satellite densities. a_p is a good indicator of the source, because JB2008 uses a_p when no
 476 storms are detected. JB2008 is overestimating the impact of the a_p fluctuations relative to
 477 HASDM and considering the satellite densities.

7 Summary

In this work, we perform scientific investigation into HASDM and JB2008 densities by leveraging PCA, and we conduct an assessment of these models relative to CHAMP and GRACE-A density estimates. To analyze the model data, PCA was applied after normalization and centering. This resulted in a useful covariance matrix and time-dependent coefficients. The covariance matrix can be examined about any axis to identify spatial features that contribute significantly to the variance in the dataset. By looking at SLT-latitude slices at 400 km, we identified key contributions to the system's variance. The most important for both models was solar heating, followed by annual variations. The third mode primarily represented the impact of geomagnetic activity. The fourth and fifth modes were difficult to discern but were flipped between the models; this means that their relative importance is different.

Next, we explored the time-dependent coefficients, or PCA scores. There were striking similarities for the first three coefficients between models, but it becomes challenging to compare for the higher-order coefficients. In the correlation analysis, most driver-coefficient combinations produced weak correlations, with the exception of α_1 . To investigate the processes at solar maximum, the window was limited to 2001. This resulted in more distinct trends in the coefficient plots, highlighting the effects of solar and geomagnetic activity along with annual and semiannual trends. JB2008 had more evident variations and subsequently higher correlations to the drivers. The HASDM coefficients had weaker signals and correlations. Relative to the 20-year analysis, the correlation figures displayed stronger correlations across a majority of coefficients. The solar drivers had non-negligible correlations with most of the coefficients due to the variance caused by EUV irradiance.

This study was performed once more on 2019, to investigate the datasets during solar minimum. The coefficients had weaker signal compared to 2001, and the correlations seen in 2001 had changed drastically. The solar drivers had less impact on the variance, and the temporal drivers had more pronounced correlations.

Last, we compared the two models to CHAMP and GRACE-A accelerometer-derived density estimates. The HASDM density distribution more closely match those of CHAMP and GRACE-A, yet both models had similar biases relative to the satellite densities. Mean absolute differences were assessed across the datasets along with yearly values. Overall,

510 HASDM's predictions were closer to CHAMP's estimates (orbit=29.35% & averaged=23.81%)
 511 than JB2008's (orbit=33.96% & averaged=27.63%). This observation was also true with
 512 respect to GRACE-A: HASDM (orbit=41.80% & averaged=30.84%) JB2008 (orbit=50.52%
 513 & averaged=39.75%).

514 We looked at both storm and quiet periods to see how well the models tracked satel-
 515 lite densities on a shorter time-scale. In general, HASDM tracked both satellites' estimates
 516 better, particularly for the orbit-averaged densities. Over the two geomagnetic storms in
 517 the 2003 Halloween storm, HASDM predicted higher peak densities than JB2008 or the
 518 satellites, but it modeled the pre- and post-storm densities well. There were spikes for
 519 JB2008's density predictions during the solar minimum/quiet period that showed an over-
 520 estimation of a_p fluctuations on density.

521 **8 Future Work**

522 In the future, we plan to develop machine-learned (ML) models on the PCA coeffi-
 523 cients using various drivers. Not only will it generate a computationally efficient predic-
 524 tive model, it will allow us to perform nonlinear analysis into the contribution of these
 525 and additional drivers to the PCA scores. These models can leverage ML techniques to
 526 also model uncertainty in the system (*Licata et al. 2021*).

527 **9 Data Statement**

528 The JB2008 model is available for download at <https://spacewx.com/jb2008/>,
 529 and requests can be submitted for access to the SET HASDM density database at <https://spacewx.com/hasdm/>. The historical space weather indices used in this study can also
 530 be found at the JB2008 link.
 531

532 Original CHAMP and GRACE density estimates from (*Mehta et al. 2017*) can be
 533 found at <http://tinyurl.com/densitysets>. As a product of this work, we appended
 534 the HASDM and JB2008 density estimates to those files. These updated files can be found
 535 at <https://zenodo.org/record/4602380#.YEW-1KhuU>

536 **10 Acknowledgements**

537 This work was made possible by NASA Established Program to Stimulate Competi-
 538 tive Research, Grant #80NSSC19M0054. SET and WVU gratefully acknowledge support

539 from the NASA SBIR contract #80NSSC20C0292 for Machine learning Enabled Thermo-
540 sphere Advanced by HASDM (META-HASDM).

541 **References**

- 542 Bettadpur, S. (2012), Gravity Recovery and Climate Experiment: Product Specification
543 Document, *GRACE 327-720, CSR-GR-03-02*, cent. for Space Res., The Univ. of Texas,
544 Austin, TX.
- 545 Bowman, B., W. K. Tobiska, F. Marcos, C. Huang, C. Lin, and W. Burke (2008), A New
546 Empirical Thermospheric Density Model JB2008 Using New Solar and Geomagnetic
547 Indices, in *AIAA/AAS Astrodynamics Specialist Conference*, AIAA 2008-6438.
- 548 Bruinsma, S., C. Boniface, E. K. Sutton, and M. Fedrizzi (2021), Thermosphere modeling
549 capabilities assessment: geomagnetic storms, *J. Space Weather Space Clim.*, *11*, 12, doi:
550 10.1051/swsc/2021002.
- 551 Bruinsma, Sean (2015), The DTM-2013 thermosphere model, *J. Space Weather Space*
552 *Clim.*, *5*, A1, doi:10.1051/swsc/2015001.
- 553 Casali, S., and W. Barker (2002), Dynamic Calibration Atmosphere (DCA) for the High
554 Accuracy Satellite Drag Model (HASDM), in *AIAA/AAS Astrodynamics Specialist Con-*
555 *ference and Exhibit*, doi:10.2514/6.2002-4888.
- 556 Covington, A. E. (1948), Solar Noise Observations on 10.7 Centimeters, *Proceedings of*
557 *the IRE*, *36*(4), 454–457, doi:10.1109/JRPROC.1948.234598.
- 558 Deng, Y., T. J. Fuller-Rowell, A. J. Ridley, D. Knipp, and R. E. Lopez (2013), Theoretical
559 study: Influence of different energy sources on the cusp neutral density enhancement,
560 *Journal of Geophysical Research: Space Physics*, *118*(5), 2340–2349, doi:https://doi.org/
561 10.1002/jgra.50197.
- 562 Doornbos, E. (2012), *Producing Density and Crosswind Data from Satellite Dynam-*
563 *ics Observations*, pp. 91–126, Springer Berlin Heidelberg, Berlin, Heidelberg, doi:
564 10.1007/978-3-642-25129-0_4.
- 565 Emmert, J. (2015), Thermospheric mass density: A review, *Advances in Space Research*,
566 *56*, doi:10.1016/j.asr.2015.05.038.
- 567 Fedrizzi, M., T. J. Fuller-Rowell, and M. V. Codrescu (2012), Global joule heating index
568 derived from thermospheric density physics-based modeling and observations, *Space*
569 *Weather*, *10*(3), doi:https://doi.org/10.1029/2011SW000724.

- 570 Ganushkina, N., A. Jaynes, and M. Liemohn (2017), Space Weather Effects Produced by
571 the Ring Current Particles, *Space Science Reviews*, 212(3-4), 1315–1344, doi:10.1007/
572 s11214-017-0412-2.
- 573 Gondelach, D. J., and R. Linares (2020), Real-Time Thermospheric Density Estimation
574 via Two-Line Element Data Assimilation, *Space Weather*, 18(2), e2019SW002,356, doi:
575 <https://doi.org/10.1029/2019SW002356>, e2019SW002356 10.1029/2019SW002356.
- 576 Jacchia, L. G. (1970), New Static Models of the Thermosphere and Exosphere with Em-
577 pirical Temperature Profiles, *SAO Special Report*, 313.
- 578 Jolliffe, I. T., and J. Cadima (2016), Principal component analysis: a review and recent
579 developments, *Philosophical Transactions of the Royal Society A: Mathematical, Physical*
580 *and Engineering Sciences*, 374(2065), 20150,202, doi:10.1098/rsta.2015.0202.
- 581 Keating, G. M., and E. J. Prior (1968), The winter helium bulge, in space research VIII,
582 in *Proceedings of the Tenth Cospar Plenary Meeting*, p. 982–992.
- 583 Kessler, D. J., and B. G. Cour-Palais (1978), Collision frequency of artificial satellites:
584 The creation of a debris belt, *Journal of Geophysical Research: Space Physics*, 83(A6),
585 2637–2646, doi:<https://doi.org/10.1029/JA083iA06p02637>.
- 586 Licata, R., P. Mehta, and W. K. Tobiska (2021), Impact of driver and model uncertainty
587 on drag and orbit prediction, in *Proceedings of the 31st AAS/AIAA Space Flight Mechan-*
588 *ics Meeting*.
- 589 Licata, R. J., W. K. Tobiska, and P. M. Mehta (2020), Benchmarking forecasting models
590 for space weather drivers, *Space Weather*, 18(10), e2020SW002,496, doi:[https://doi.org/](https://doi.org/10.1029/2020SW002496)
591 [10.1029/2020SW002496](https://doi.org/10.1029/2020SW002496), e2020SW002496 10.1029/2020SW002496.
- 592 Luhr, H., L. Grunwaldt, and C. Forste (2002), CHAMP Reference Systems, Transforma-
593 tions and Standards, *Tech. rep.*, CH-GFZ-RS-002, GFZ-Potsdam, Postdam, Germany.
- 594 Marcos, F., M. Kendra, J. Griffin, J. Bass, D. Larson, and J. J. Liu (1998), Precision Low
595 Earth Orbit Determination Using Atmospheric Density Calibration, *Journal of The As-*
596 *tronautical Sciences*, 46, 395–409.
- 597 McClain, W., and D. Vallado (2001), *Fundamentals of Astrodynamics and Applications*,
598 Space Technology Library, 556-557 pp., Springer Netherlands.
- 599 Mehta, P. M., and R. Linares (2017), A methodology for reduced order modeling and
600 calibration of the upper atmosphere, *Space Weather*, 15(10), 1270–1287, doi:10.1002/
601 2017SW001642.

- 602 Mehta, P. M., A. C. Walker, E. K. Sutton, and H. C. Godinez (2017), New density esti-
603 mates derived using accelerometers on board the CHAMP and GRACE satellites, *Space*
604 *Weather*, *15*(4), 558–576, doi:<https://doi.org/10.1002/2016SW001562>.
- 605 Mehta, P. M., R. Linares, and E. K. Sutton (2018), A Quasi-Physical Dynamic Reduced
606 Order Model for Thermospheric Mass Density via Hermitian Space-Dynamic Mode
607 Decomposition, *Space Weather*, *16*(5), 569–588, doi:10.1029/2018SW001840.
- 608 Mehta, P. M., R. Linares, and E. K. Sutton (2019), Data-Driven Inference of Thermo-
609 sphere Composition During Solar Minimum Conditions, *Space Weather*, *17*(9), 1364–
610 1379, doi:<https://doi.org/10.1029/2019SW002264>.
- 611 Nazarenko, A., P. Cefola, and V. Yurasov (1998), Estimating atmospheric density varia-
612 tions to improve LEO orbit prediction accuracy, in *AIAA/AAS Space Flight Mechanics*
613 *Meeting*, AAS 98-190.
- 614 Picone, J. M., A. E. Hedin, D. P. Drob, and A. C. Aikin (2002), NRLMSISE-00 em-
615 pirical model of the atmosphere: Statistical comparisons and scientific issues, *Jour-*
616 *nal of Geophysical Research: Space Physics*, *107*(A12), SIA 15–1–SIA 15–16, doi:
617 10.1029/2002JA009430.
- 618 Qian, L., and S. Solomon (2011), Thermospheric density: An overview of temporal and
619 spatial variations, *Space Science Reviews - SPACE SCI REV*, *168*, 1–27, doi:10.1007/
620 s11214-011-9810-z.
- 621 Reber, C. A., and P. B. Hays (1973), Thermospheric wind effects on the distribution of
622 helium and argon in the Earth’s upper atmosphere, *Journal of Geophysical Research*
623 *(1896-1977)*, *78*(16), 2977–2991, doi:<https://doi.org/10.1029/JA078i016p02977>.
- 624 Schober, P., C. Boer, and L. Schwarte (2018), Correlation Coefficients: Appropriate
625 Use and Interpretation, *Anesthesia & Analgesia*, *126*, 1763–1768, doi:10.1213/ANE.
626 0000000000002864.
- 627 Storz, M., B. Bowman, and J. Branson (2005), High Accuracy Satellite Drag Model
628 (HASDM), in *AIAA/AAS Astrodynamics Specialist Conference and Exhibit*, doi:10.2514/
629 6.2002-4886.
- 630 Sutton, E. K. (2008), Effects of solar disturbances on the thermosphere densities and
631 winds from CHAMP and GRACE satellite accelerometer data, Ph.D. thesis, University
632 of Colorado at Boulder.
- 633 Tobiska, W., T. Woods, F. Eparvier, R. Viereck, L. Floyd, D. Bouwer, G. Rottman, and
634 O. White (2000), The SOLAR2000 empirical solar irradiance model and forecast tool,

- 635 *Journal of Atmospheric and Solar-Terrestrial Physics*, 62(14), 1233 – 1250, doi:https:
636 //doi.org/10.1016/S1364-6826(00)00070-5.
- 637 Tobiska, W. K., S. D. Bouwer, and B. R. Bowman (2008a), The development of new solar
638 indices for use in thermospheric density modeling, *Journal of Atmospheric and Solar-*
639 *Terrestrial Physics*, 70(5), 803–819, doi:https://doi.org/10.1016/j.jastp.2007.11.001.
- 640 Tobiska, W. K., B. Bowman, and S. D. Bouwer (2008b), *Solar and Geomagnetic Indices*
641 *for the JB2008 Thermosphere Density Model*, chap. 4, COSPAR CIRA Draft.
- 642 Tobiska, W. K., D. Knipp, W. J. Burke, D. Bouwer, J. Bailey, D. Odstrcil, M. P. Hagan,
643 J. Gannon, and B. R. Bowman (2013), The Anemomilos prediction methodology for
644 Dst, *Space Weather*, 11(9), 490–508, doi:10.1002/swe.20094.
- 645 Tobiska, W. K., B. R. Bowman, D. Bouwer, A. Cruz, K. Wahl, M. Pilinski, P. M. Mehta,
646 and R. J. Licata (2021), The SET HASDM density database, *Space Weather*, p.
647 e2020SW002682, doi:https://doi.org/10.1029/2020SW002682.
- 648 Vickers, H., M. J. Kosch, E. Sutton, L. Bjoland, Y. Ogawa, and C. La Hoz (2014), A solar
649 cycle of upper thermosphere density observations from the eiscat svalbard radar, *Jour-*
650 *nal of Geophysical Research: Space Physics*, 119(8), 6833–6845, doi:https://doi.org/10.
651 1002/2014JA019885.

Figure 1.

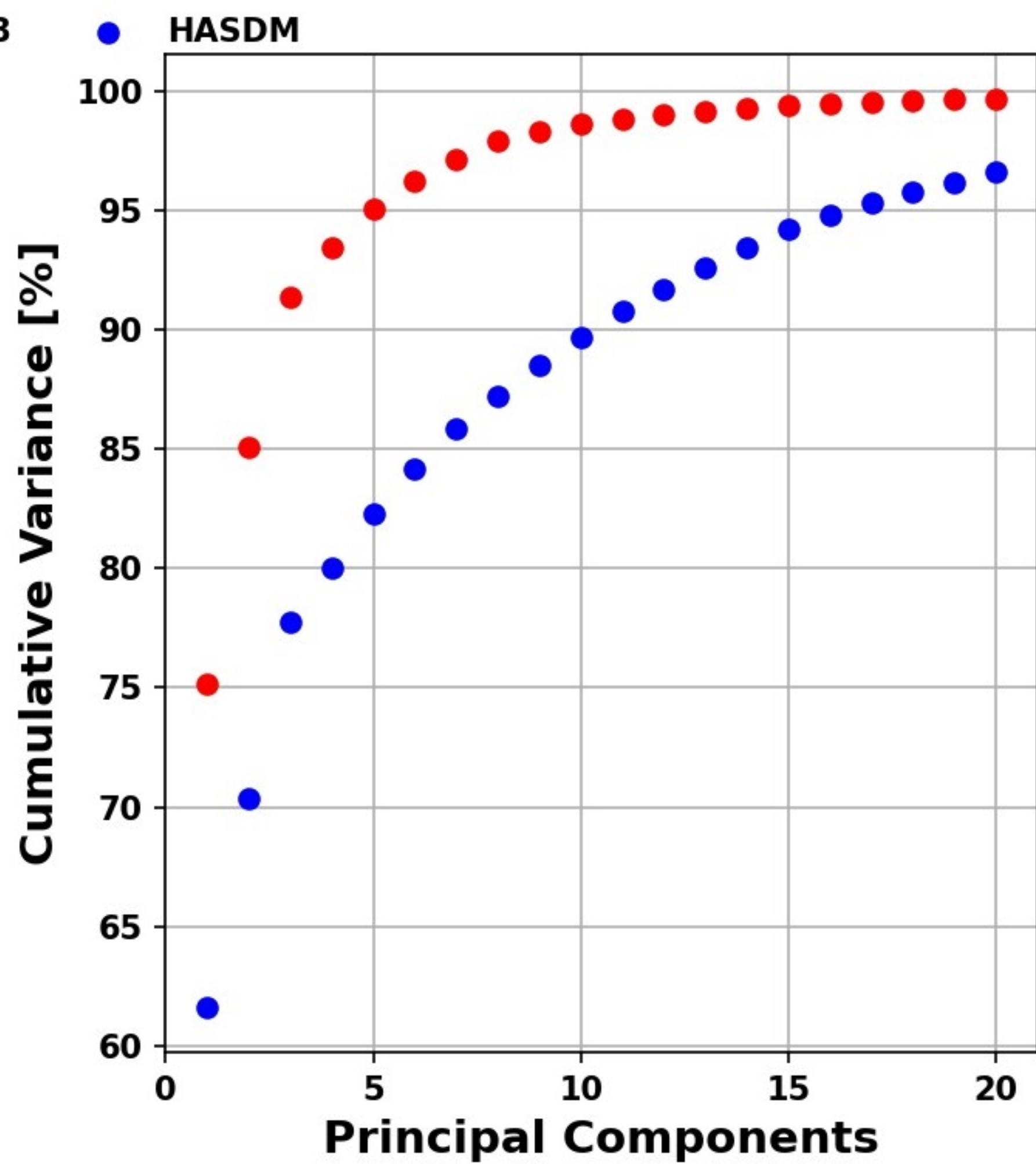
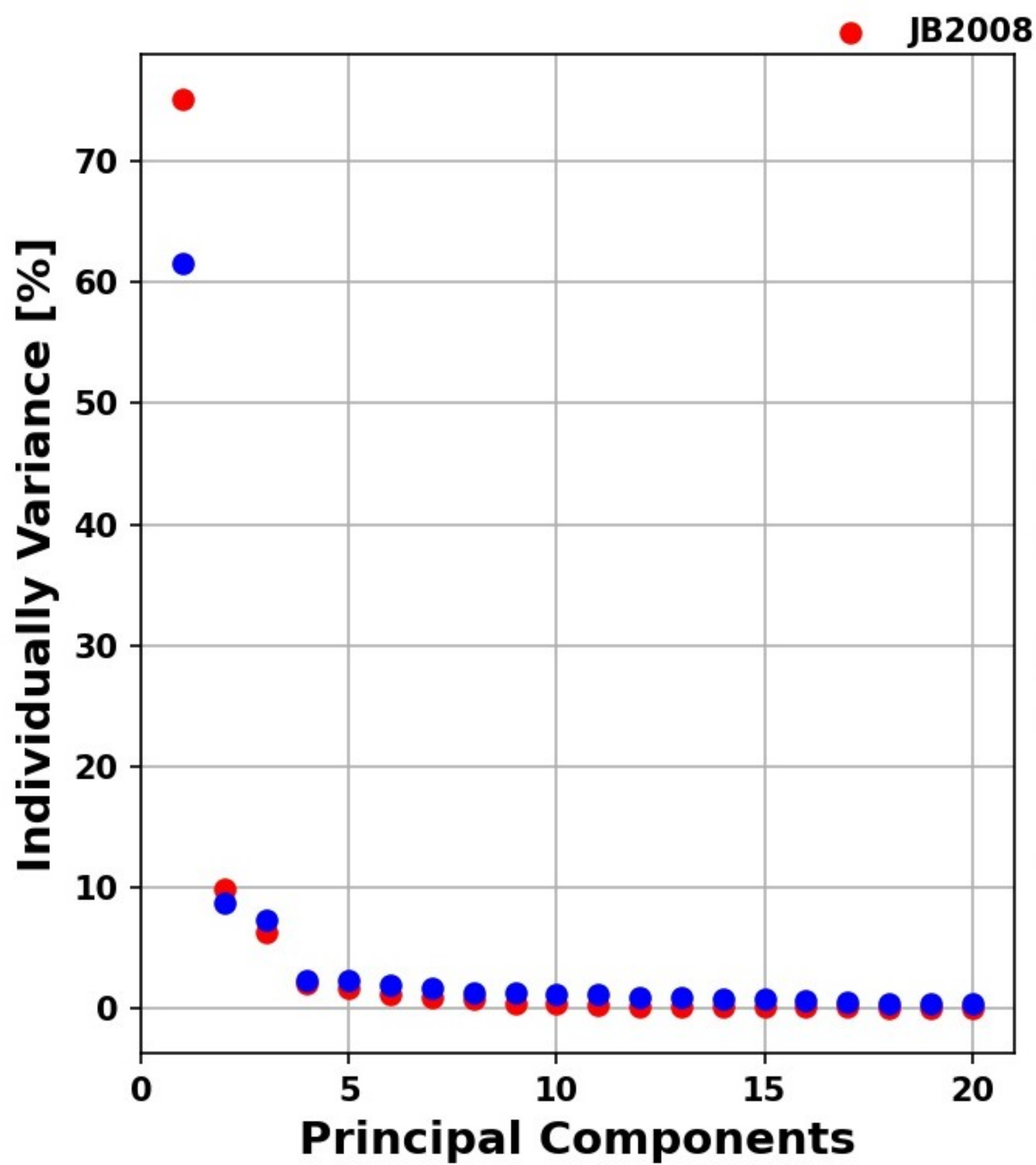


Figure 2.

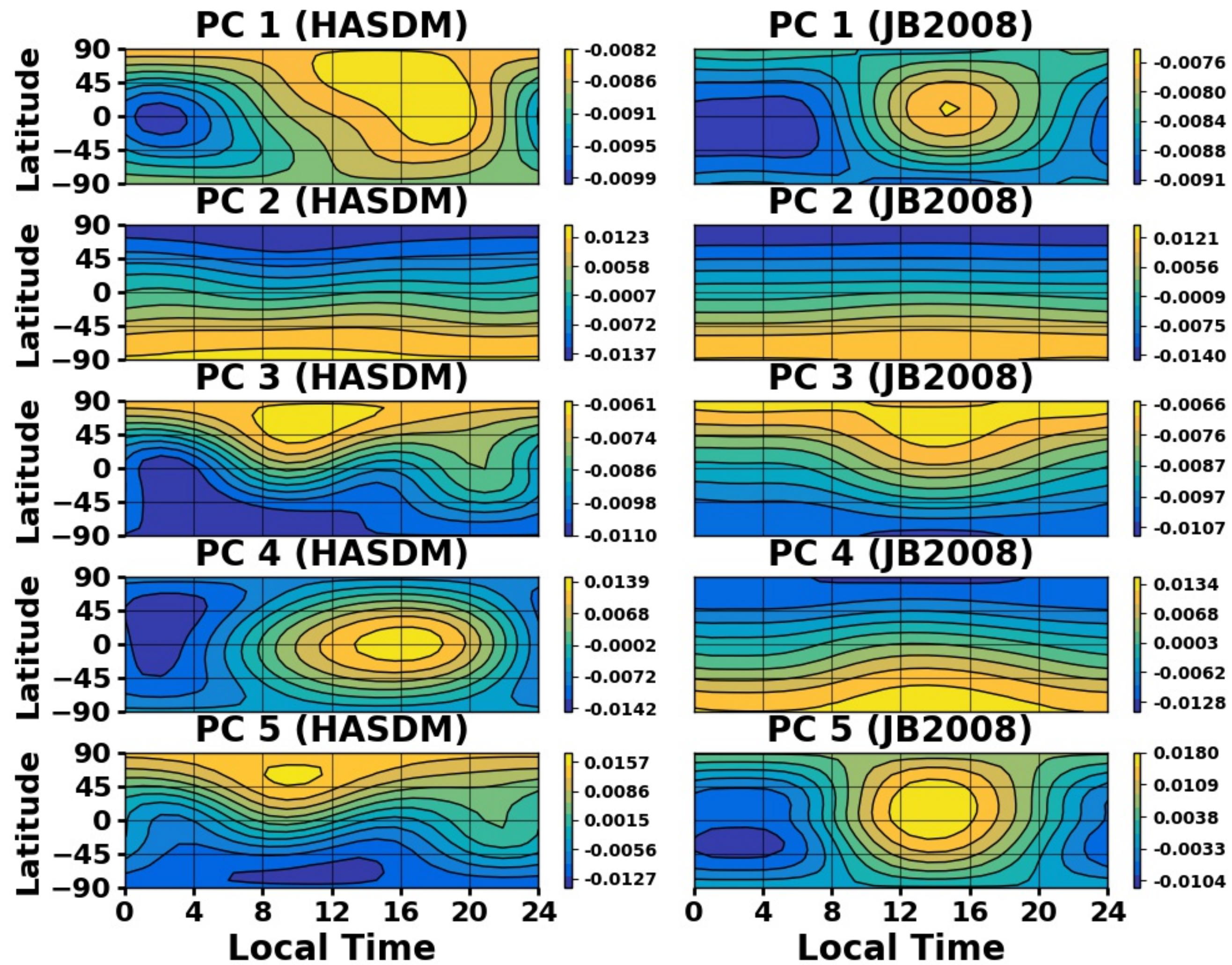


Figure 3.

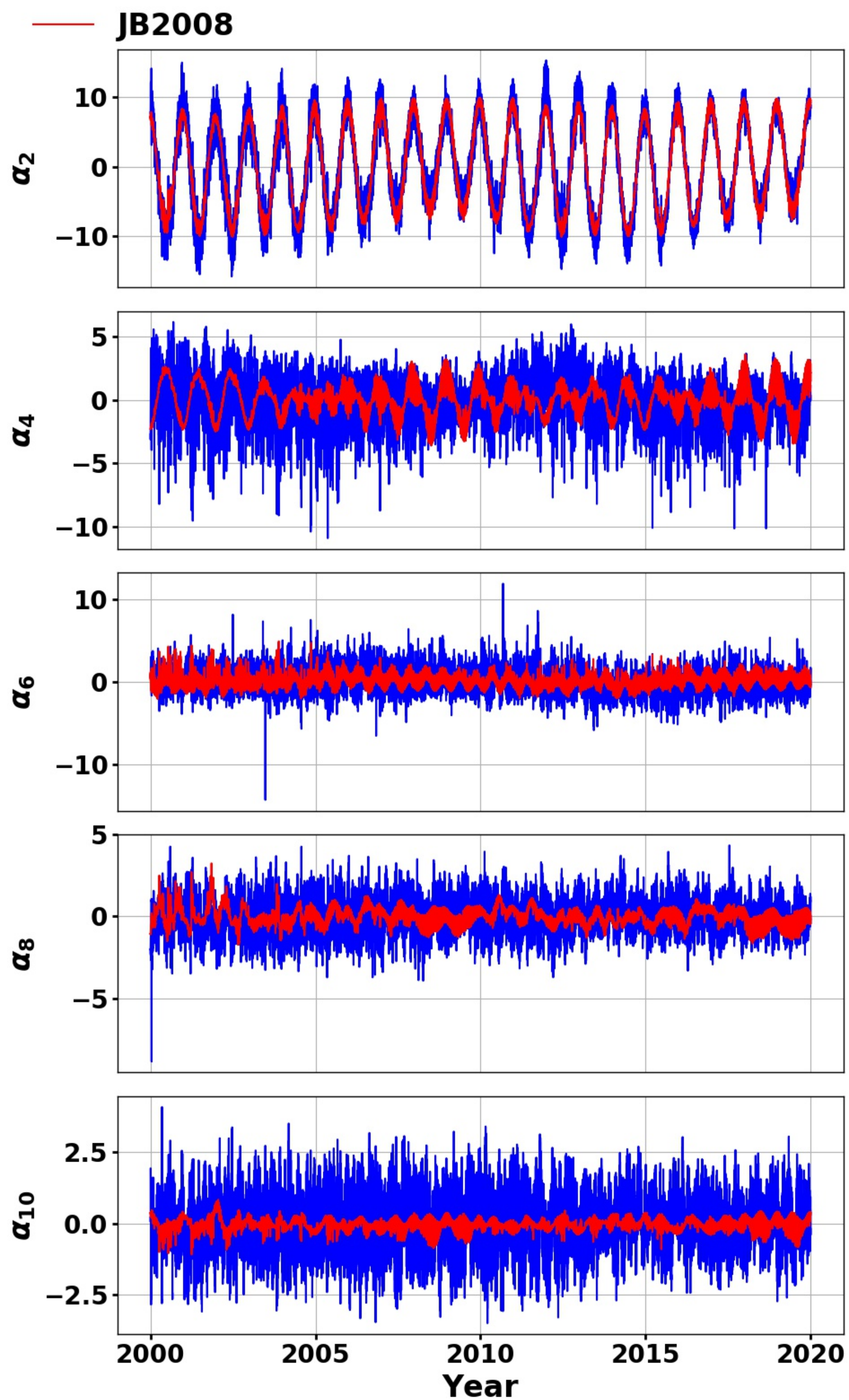
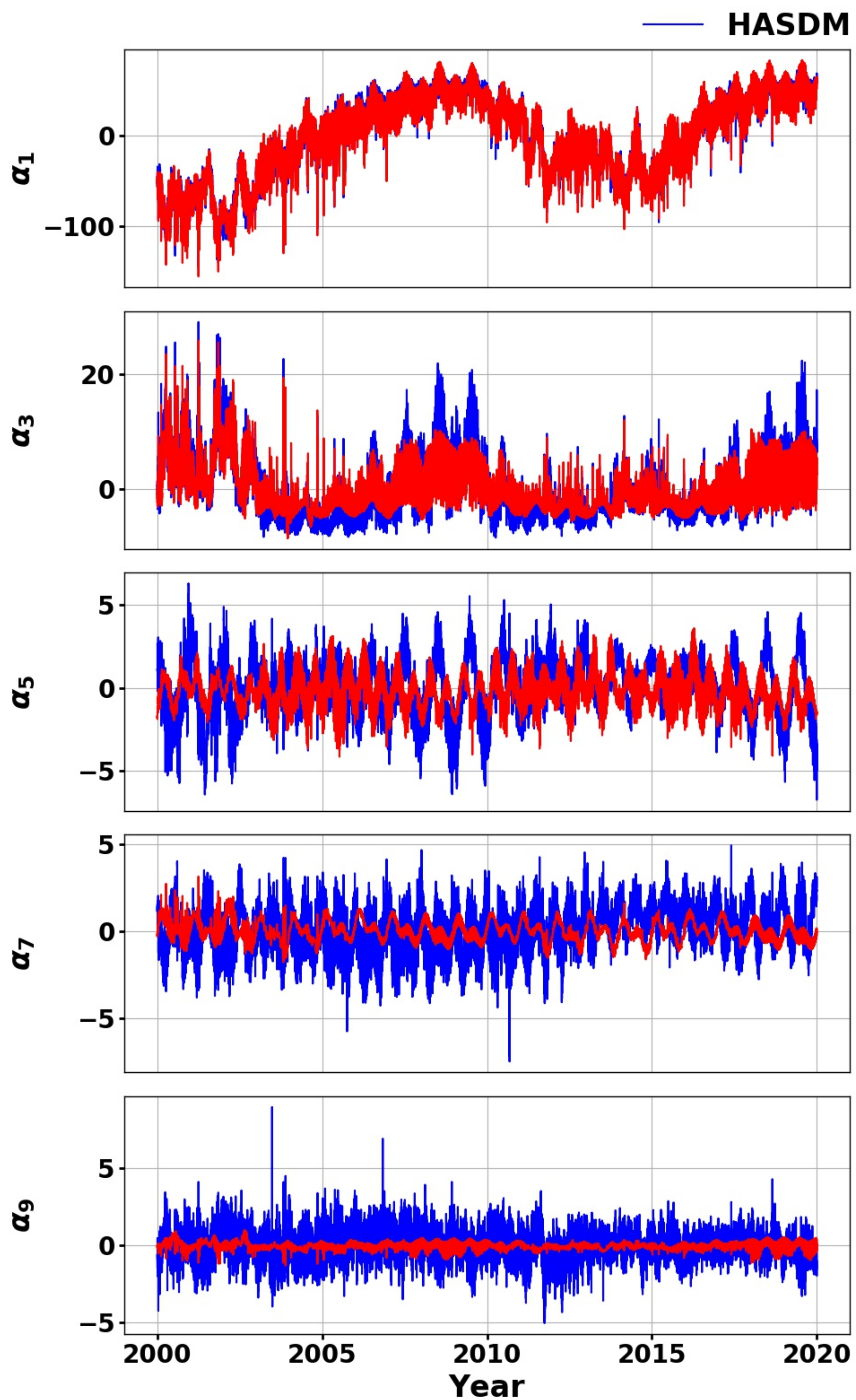


Figure 4.

HASDM(2000 – 2020)

	α_1	α_2	α_3	α_4	α_5	α_6	α_7	α_8	α_9	α_{10}
F_{10}	-0.91	-0.04	0.20	0.15	-0.02	0.01	0.03	-0.00	0.04	0.00
F_{81c}	-0.94	-0.04	0.16	0.15	-0.00	0.02	0.02	-0.01	0.02	-0.01
S_{10}	-0.96	-0.09	0.07	0.17	0.01	0.02	0.04	0.00	0.02	0.00
S_{81c}	-0.95	-0.09	0.04	0.16	0.02	0.03	0.03	-0.00	0.01	-0.01
M_{10}	-0.94	-0.09	0.16	0.16	-0.00	0.00	0.06	-0.01	0.03	0.01
M_{81c}	-0.94	-0.09	0.12	0.14	0.01	0.01	0.06	-0.01	0.01	-0.01
Y_{10}	-0.94	-0.10	0.02	0.15	0.03	0.01	0.08	-0.02	-0.02	-0.00
Y_{81c}	-0.94	-0.10	0.00	0.14	0.04	0.01	0.07	-0.02	-0.02	-0.02
ap	-0.26	-0.04	0.00	-0.47	-0.04	0.08	0.05	-0.01	0.01	-0.03
Dst	0.34	-0.01	-0.01	0.51	0.06	0.15	0.10	0.01	-0.09	0.03
semi _{sin}	0.06	-0.01	0.01	0.04	0.01	0.09	-0.04	0.01	-0.01	-0.03
semi _{cos}	0.11	0.05	0.13	0.09	0.18	0.01	0.58	-0.06	0.05	-0.11
ann _{sin}	-0.04	-0.17	-0.03	-0.03	-0.06	0.00	-0.05	-0.09	0.00	-0.05
ann _{cos}	-0.14	0.94	-0.10	0.00	-0.14	0.00	-0.01	-0.02	0.01	0.00

JB2008(2000 – 2020)

	α_1	α_2	α_3	α_4	α_5	α_6	α_7	α_8	α_9	α_{10}
F_{10}	-0.90	-0.03	0.18	-0.01	-0.01	-0.19	-0.07	0.02	0.11	0.07
F_{81c}	-0.92	-0.04	0.13	-0.02	-0.02	-0.16	-0.03	-0.02	0.10	0.09
S_{10}	-0.95	-0.08	0.06	-0.01	0.01	-0.19	-0.02	0.01	0.06	0.05
S_{81c}	-0.94	-0.08	0.02	-0.01	0.02	-0.17	-0.00	-0.01	0.05	0.05
M_{10}	-0.93	-0.08	0.13	-0.01	-0.02	-0.18	-0.04	-0.01	0.08	0.07
M_{81c}	-0.93	-0.09	0.09	-0.02	-0.01	-0.15	-0.02	-0.04	0.07	0.08
Y_{10}	-0.93	-0.10	-0.00	-0.01	-0.03	-0.18	-0.06	0.00	0.04	0.03
Y_{81c}	-0.93	-0.10	-0.02	-0.01	-0.02	-0.15	-0.03	-0.02	0.04	0.04
ap	-0.25	-0.05	0.02	0.01	-0.18	0.31	0.06	0.01	-0.12	-0.14
Dst	0.35	-0.01	-0.08	0.01	0.21	-0.42	-0.07	-0.06	0.14	0.14
semi _{sin}	0.07	-0.00	-0.09	-0.10	-0.23	-0.49	0.57	-0.14	-0.01	-0.08
semi _{cos}	0.12	0.02	-0.03	-0.17	-0.69	-0.06	0.05	0.11	0.10	0.14
ann _{sin}	-0.06	-0.18	0.00	0.04	0.16	0.09	0.65	-0.33	0.00	0.07
ann _{cos}	-0.14	0.97	-0.07	0.02	0.03	0.01	0.12	-0.05	-0.03	0.05

Figure 5.

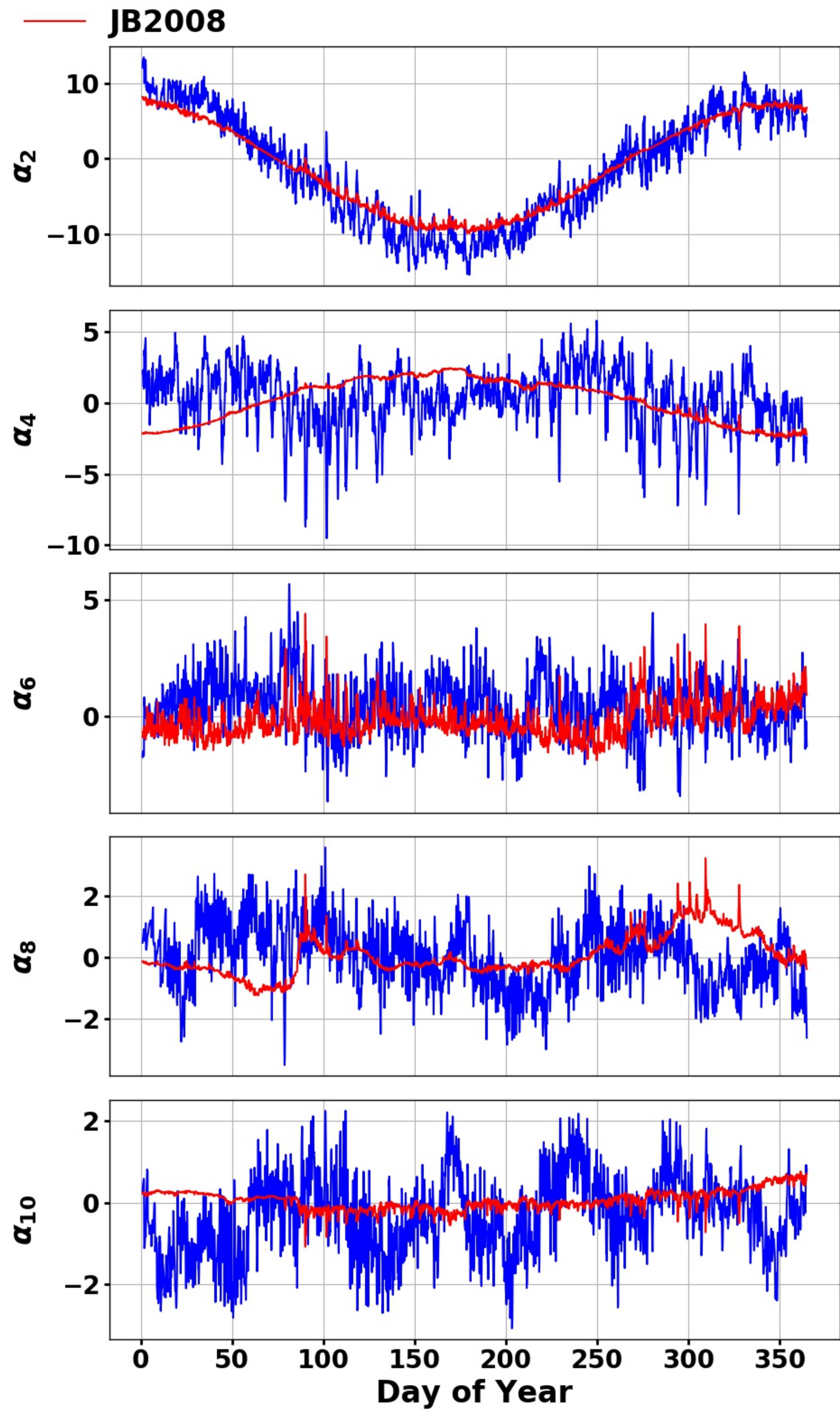
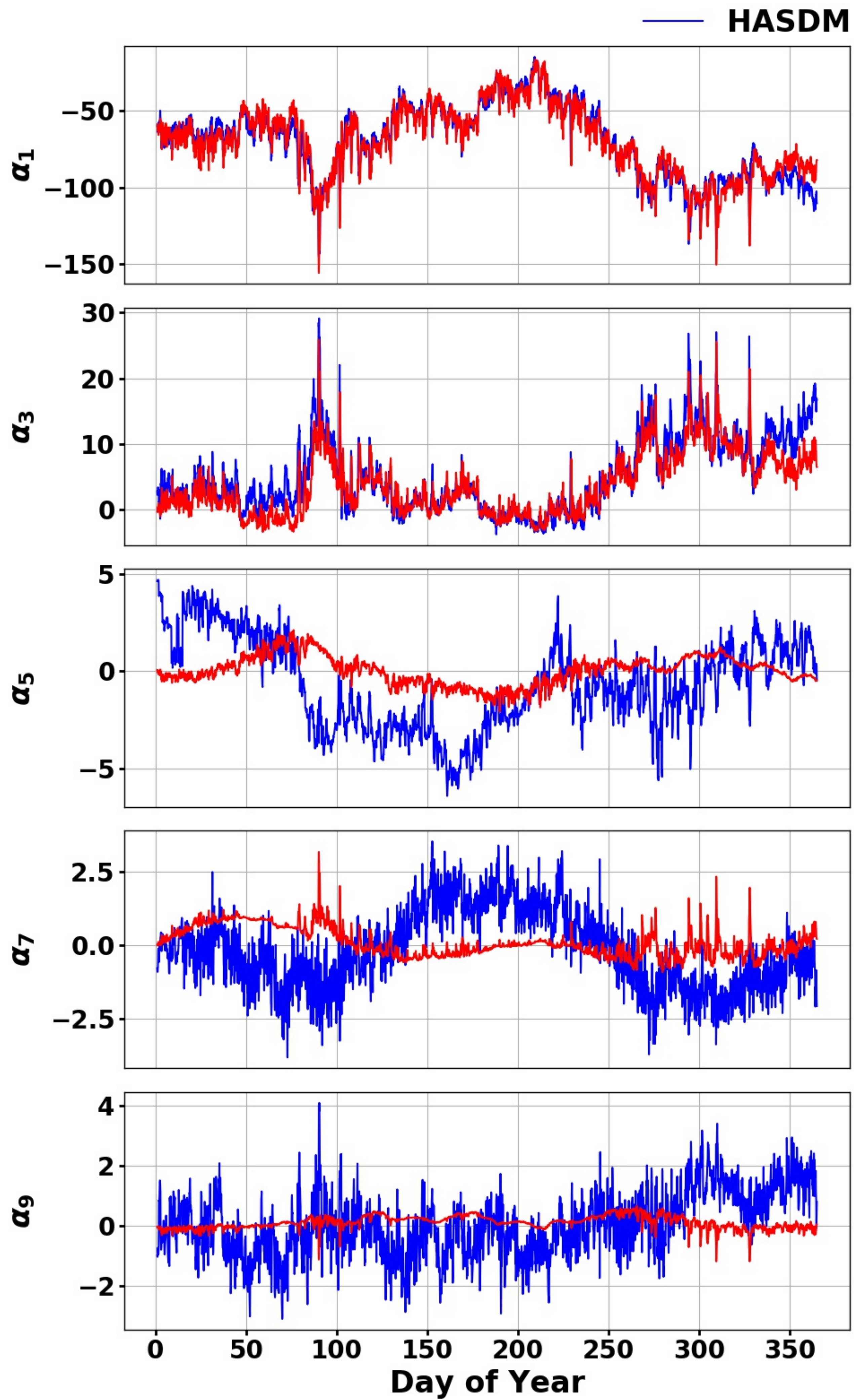


Figure 6.

HASDM(2001)

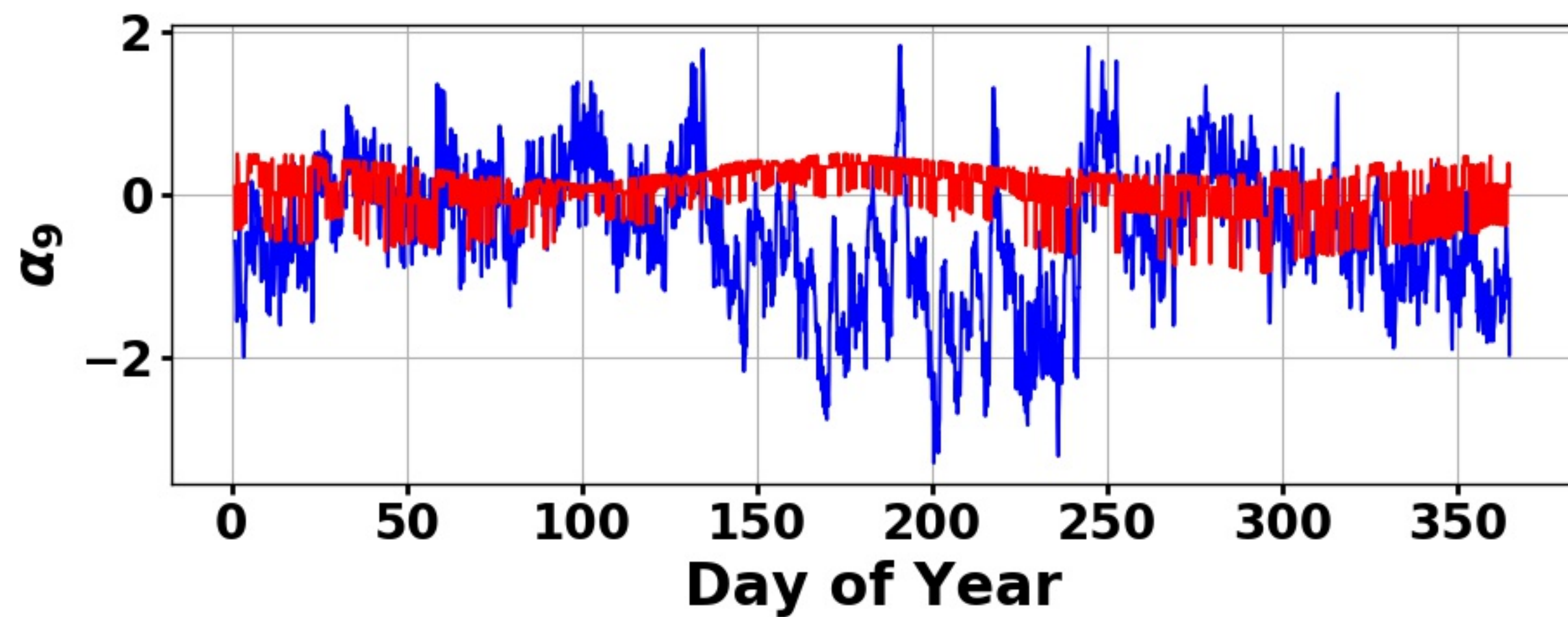
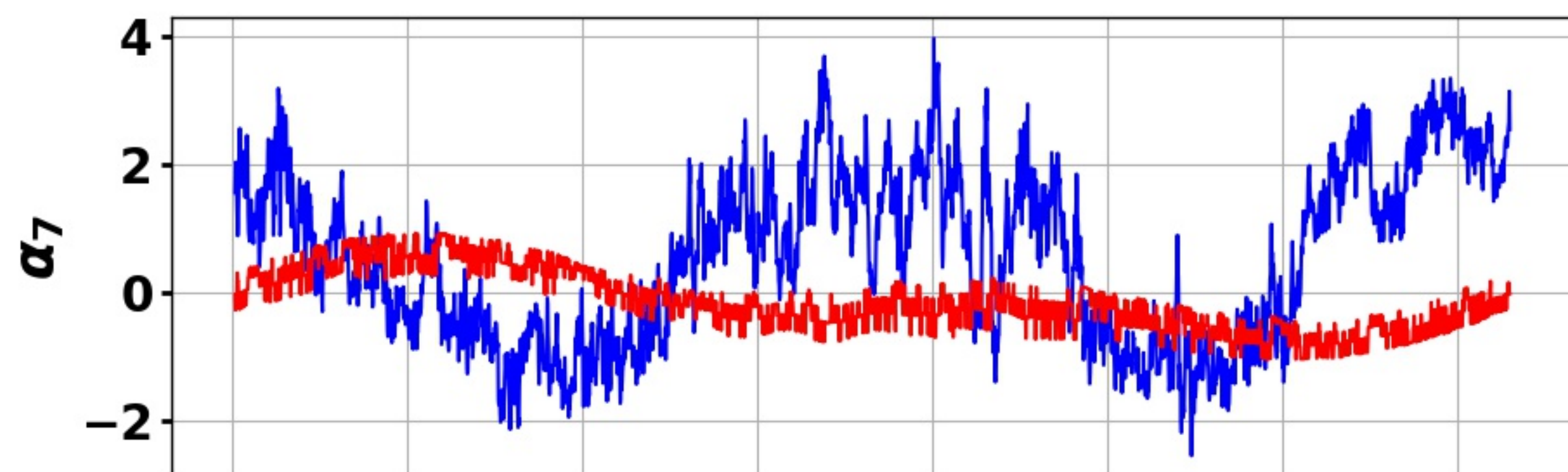
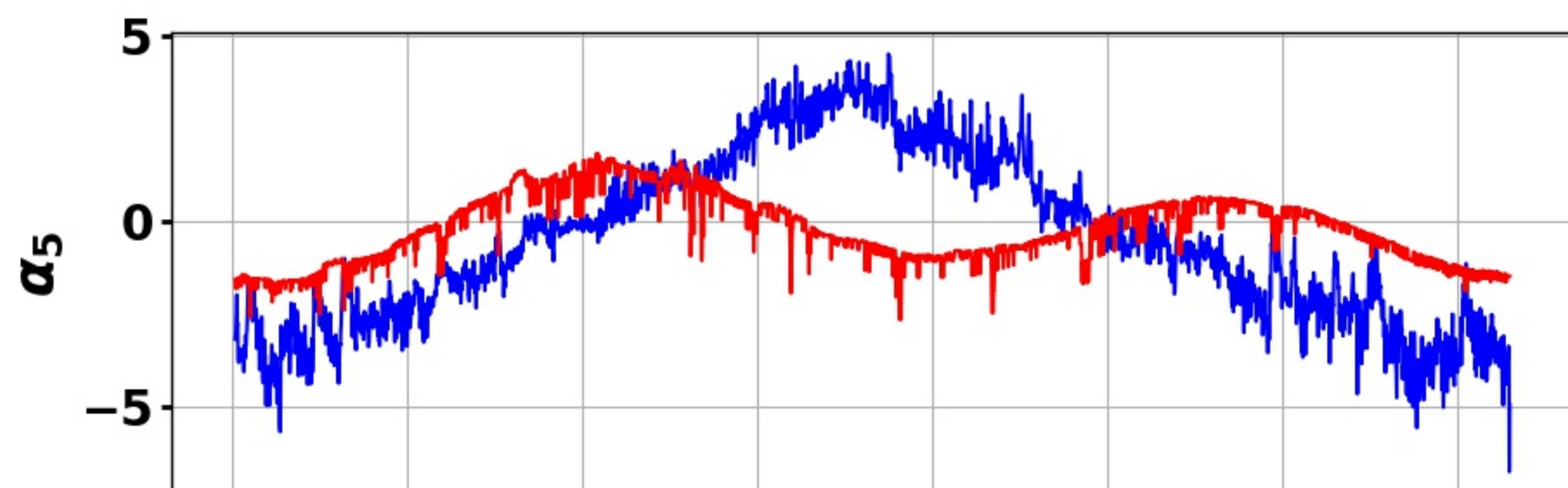
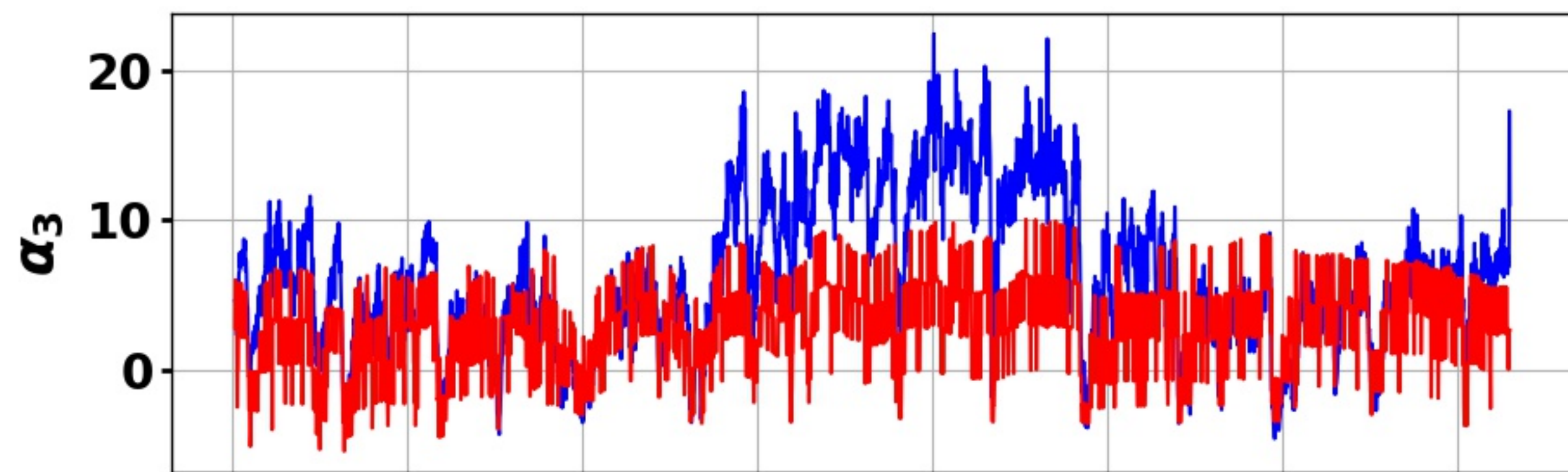
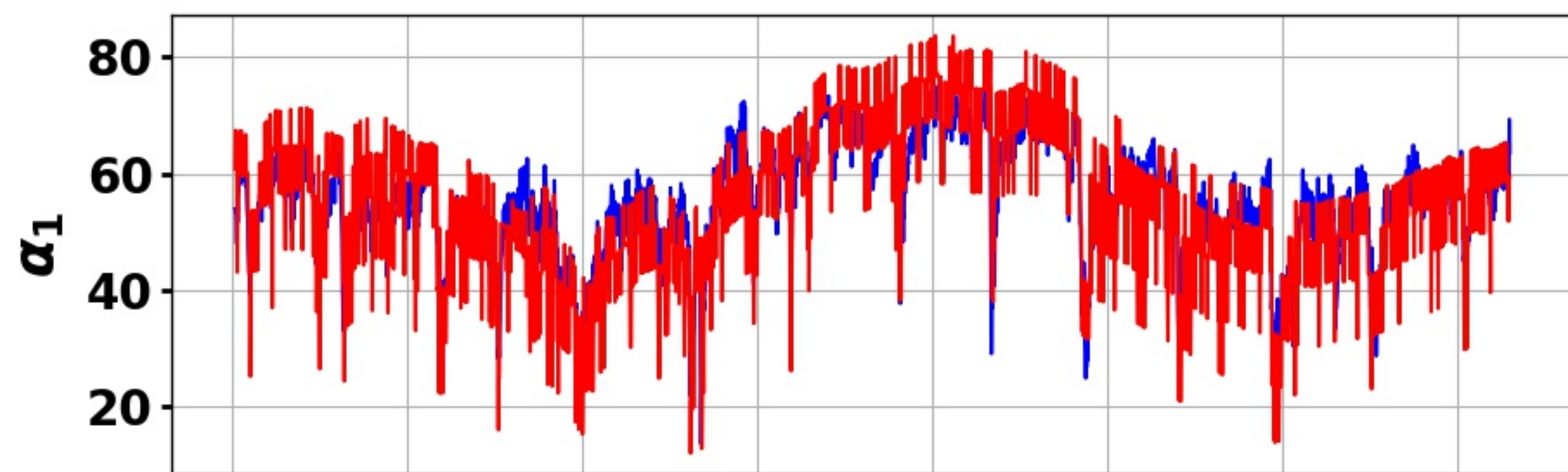
	α_1	α_2	α_3	α_4	α_5	α_6	α_7	α_8	α_9	α_{10}
F ₁₀	-0.77	0.37	0.77	-0.17	0.01	-0.06	-0.48	-0.01	0.54	0.27
F _{81c}	-0.75	0.52	0.72	-0.18	0.18	-0.14	-0.59	-0.06	0.58	0.20
S ₁₀	-0.86	0.48	0.86	-0.24	0.07	-0.08	-0.54	-0.01	0.61	0.24
S _{81c}	-0.77	0.63	0.73	-0.18	0.29	-0.12	-0.60	-0.07	0.60	0.14
M ₁₀	-0.76	0.41	0.78	-0.20	0.05	-0.12	-0.41	-0.07	0.57	0.17
M _{81c}	-0.69	0.57	0.68	-0.16	0.26	-0.14	-0.49	-0.15	0.60	0.12
Y ₁₀	-0.73	0.35	0.73	-0.14	-0.00	-0.02	-0.44	-0.01	0.51	0.30
Y _{81c}	-0.75	0.54	0.72	-0.17	0.21	-0.14	-0.60	-0.05	0.58	0.20
ap	-0.35	0.04	0.42	-0.54	-0.10	-0.04	-0.15	-0.02	0.14	0.10
Dst	0.56	-0.17	-0.57	0.64	0.10	0.30	0.44	-0.00	-0.33	-0.19
semi _{sin}	0.41	0.07	-0.41	0.34	0.41	0.15	0.19	0.09	-0.31	-0.06
semi _{cos}	0.40	-0.02	-0.31	0.09	0.16	-0.05	0.54	-0.35	-0.00	-0.29
ann _{sin}	0.21	-0.12	-0.26	-0.09	-0.05	0.13	0.06	0.26	-0.35	-0.21
ann _{cos}	-0.59	0.95	0.49	-0.08	0.74	0.03	-0.62	0.12	0.38	-0.11

JB2008(2001)

	α_1	α_2	α_3	α_4	α_5	α_6	α_7	α_8	α_9	α_{10}
F ₁₀	-0.74	0.43	0.74	-0.35	0.40	0.28	-0.15	0.66	0.06	0.32
F _{81c}	-0.72	0.61	0.71	-0.59	0.36	0.39	-0.30	0.70	-0.14	0.57
S ₁₀	-0.83	0.55	0.83	-0.48	0.38	0.40	-0.08	0.72	-0.05	0.41
S _{81c}	-0.73	0.72	0.70	-0.70	0.35	0.41	-0.23	0.67	-0.24	0.66
M ₁₀	-0.73	0.48	0.76	-0.44	0.23	0.34	-0.14	0.68	-0.02	0.40
M _{81c}	-0.65	0.65	0.67	-0.67	0.21	0.40	-0.31	0.67	-0.23	0.66
Y ₁₀	-0.71	0.41	0.69	-0.33	0.40	0.26	-0.13	0.60	0.06	0.29
Y _{81c}	-0.72	0.62	0.70	-0.60	0.38	0.38	-0.27	0.68	-0.15	0.58
ap	-0.30	0.01	0.34	0.06	0.08	0.41	0.28	0.24	-0.23	-0.24
Dst	0.60	-0.19	-0.64	0.10	-0.21	-0.67	-0.35	-0.51	0.41	0.21
semi _{sin}	0.42	0.00	-0.51	-0.02	0.05	-0.41	0.47	-0.57	-0.03	0.03
semi _{cos}	0.41	-0.01	-0.32	-0.16	-0.70	-0.03	-0.09	-0.26	-0.29	0.24
ann _{sin}	0.23	-0.16	-0.37	0.22	0.09	-0.07	0.49	-0.54	-0.07	-0.29
ann _{cos}	-0.57	0.98	0.35	-0.96	0.51	0.22	0.38	0.21	-0.58	0.74

Figure 7.

— HASDM



— JB2008

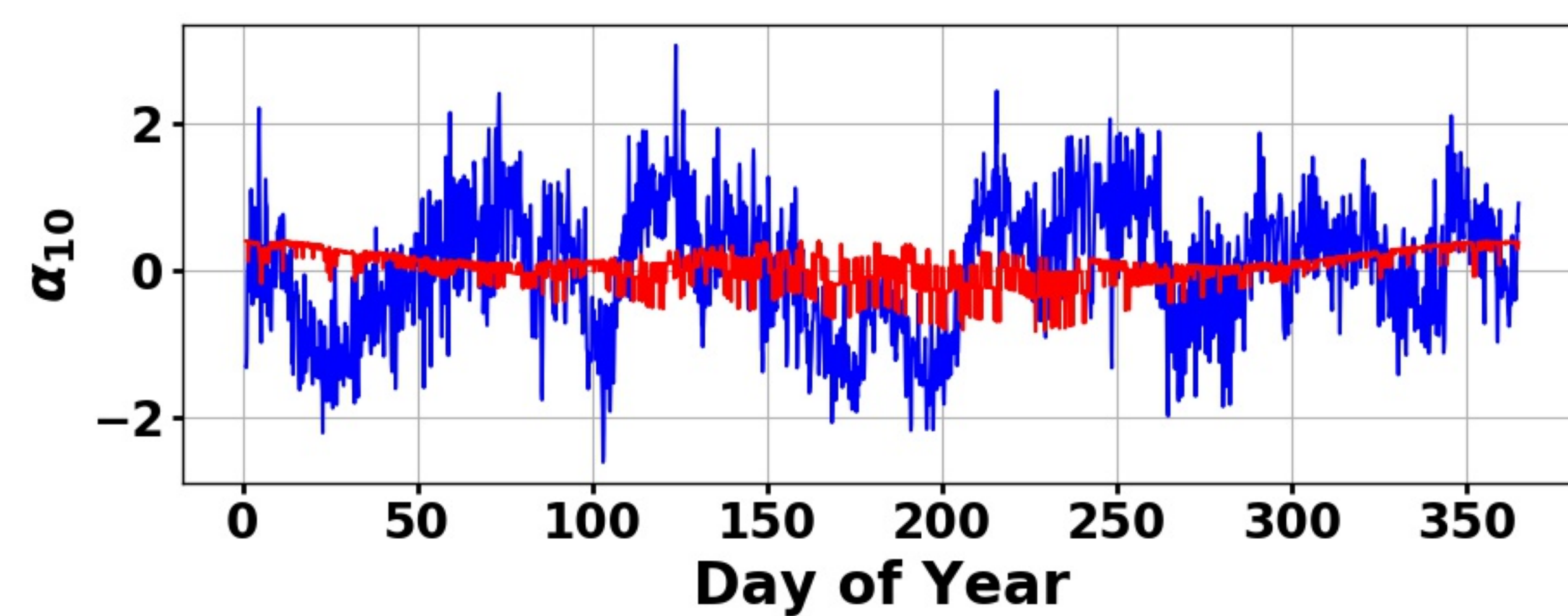
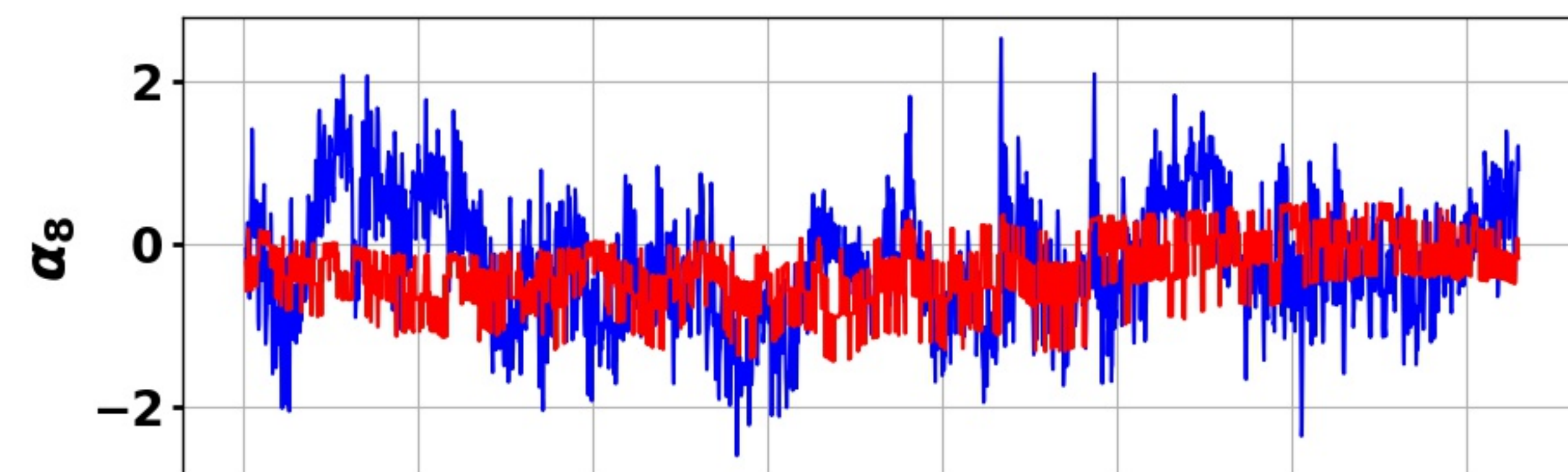
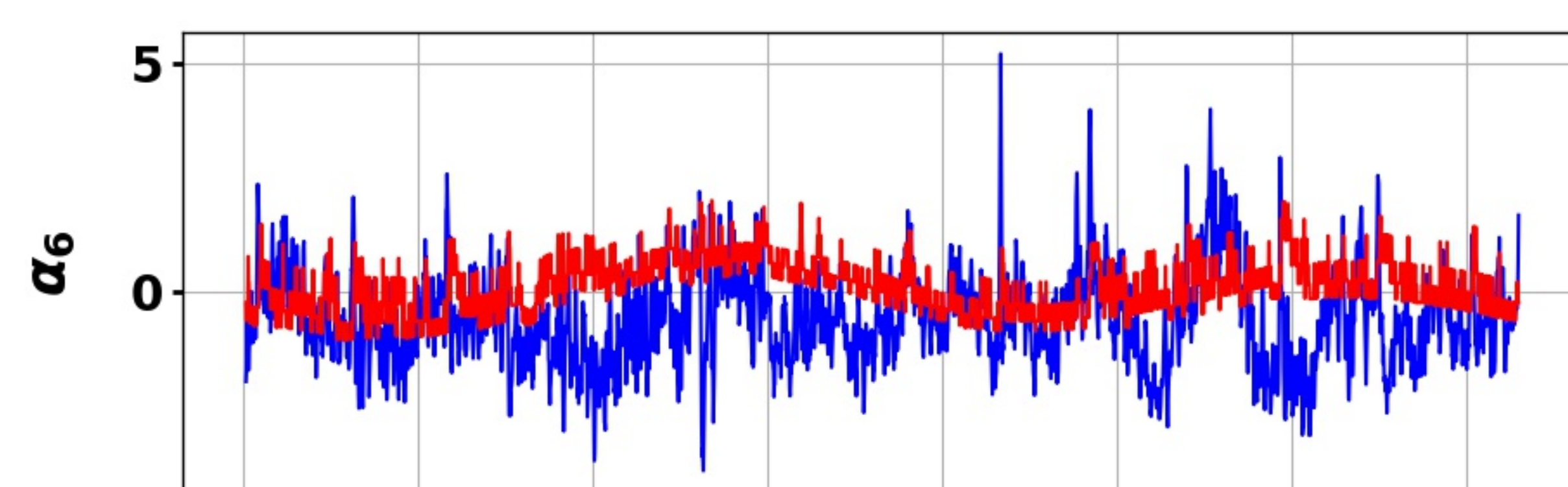
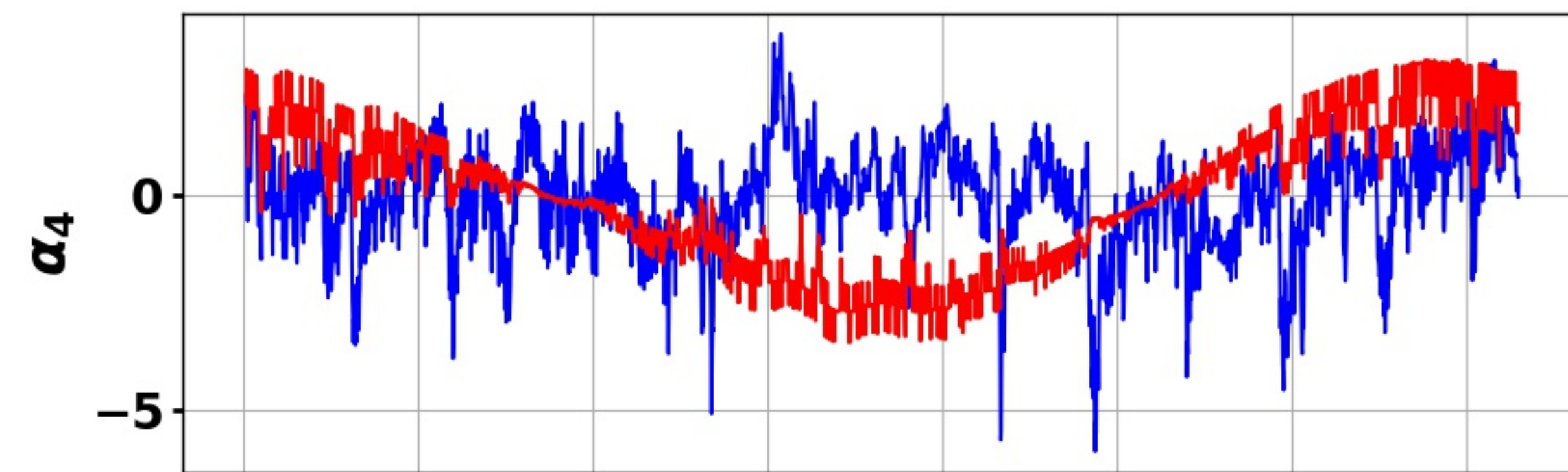
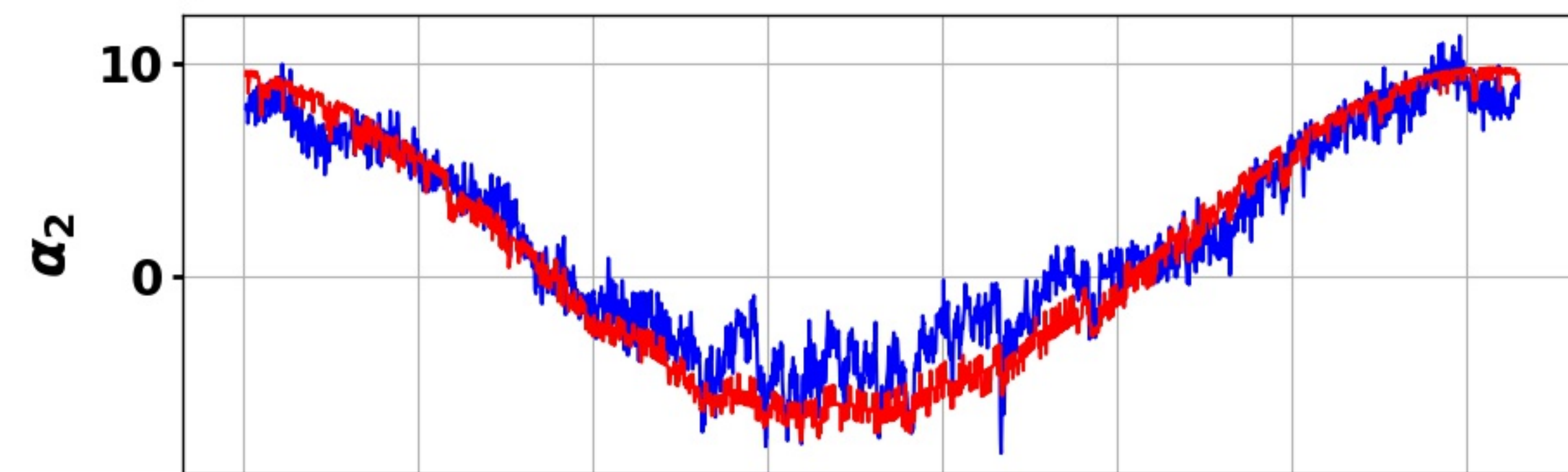


Figure 8.

HASDM(2019)

	α_1	α_2	α_3	α_4	α_5	α_6	α_7	α_8	α_9	α_{10}
F_{10}	-0.43	0.21	-0.45	0.09	-0.31	-0.15	-0.11	0.05	0.33	-0.05
F_{81c}	-0.43	0.36	-0.51	0.06	-0.46	-0.11	-0.12	0.03	0.31	0.06
S_{10}	-0.33	-0.25	-0.27	0.08	0.17	-0.14	-0.13	-0.14	0.28	-0.05
S_{81c}	-0.22	-0.34	-0.17	0.08	0.28	-0.08	-0.02	-0.28	0.13	0.06
M_{10}	-0.17	-0.32	-0.08	0.12	0.27	-0.10	-0.02	-0.18	0.12	-0.02
M_{81c}	0.00	-0.59	0.11	0.05	0.58	-0.04	0.08	-0.39	-0.06	0.11
Y_{10}	0.15	-0.28	0.24	0.16	0.34	-0.04	0.36	-0.20	-0.26	0.08
Y_{81c}	0.22	-0.36	0.32	0.13	0.44	0.01	0.39	-0.30	-0.31	0.06
ap	-0.45	-0.10	-0.36	-0.51	0.07	0.25	-0.15	0.12	0.26	-0.02
Dst	0.58	0.03	0.50	0.49	0.02	0.06	0.28	-0.13	-0.41	-0.07
semi _{sin}	0.22	0.03	0.19	-0.07	-0.04	0.05	-0.17	0.26	-0.04	-0.05
semi _{cos}	0.45	0.08	0.49	0.31	0.08	0.07	0.80	-0.01	-0.48	-0.31
ann _{sin}	-0.17	-0.19	-0.16	0.09	0.10	-0.10	-0.14	-0.09	0.19	-0.07
ann _{cos}	-0.37	0.95	-0.51	0.04	-0.95	-0.05	0.06	0.31	0.21	0.02

JB2008(2019)

	α_1	α_2	α_3	α_4	α_5	α_6	α_7	α_8	α_9	α_{10}
F_{10}	-0.37	0.23	-0.24	0.32	0.17	0.03	0.38	0.06	-0.09	0.31
F_{81c}	-0.43	0.37	-0.22	0.45	0.20	0.08	0.57	-0.09	-0.13	0.40
S_{10}	-0.33	-0.21	-0.16	-0.07	0.37	0.31	0.02	0.08	0.09	0.14
S_{81c}	-0.33	-0.34	-0.02	-0.17	0.55	0.52	0.02	-0.16	0.12	0.08
M_{10}	-0.16	-0.29	-0.02	-0.17	0.31	0.23	-0.17	0.06	0.05	-0.01
M_{81c}	-0.14	-0.60	0.14	-0.45	0.54	0.54	-0.36	-0.10	0.17	-0.16
Y_{10}	0.09	-0.29	0.22	-0.23	0.08	0.27	-0.58	0.07	0.07	-0.06
Y_{81c}	0.11	-0.38	0.27	-0.31	0.12	0.37	-0.72	0.09	0.11	-0.12
ap	-0.30	-0.07	-0.37	-0.06	-0.05	0.28	0.16	0.27	0.17	0.04
Dst	0.42	0.02	0.48	-0.00	0.06	-0.33	-0.22	-0.39	-0.19	-0.13
semi _{sin}	0.35	0.01	-0.10	-0.13	-0.39	-0.59	0.55	-0.17	0.03	-0.20
semi _{cos}	0.54	0.04	0.11	-0.08	-0.76	-0.13	-0.06	-0.10	0.30	0.26
ann _{sin}	-0.17	-0.20	-0.18	-0.13	0.27	0.10	0.70	-0.39	0.16	0.10
ann _{cos}	-0.29	0.98	-0.15	0.94	-0.31	-0.20	0.20	0.29	-0.36	0.57

Figure 9.

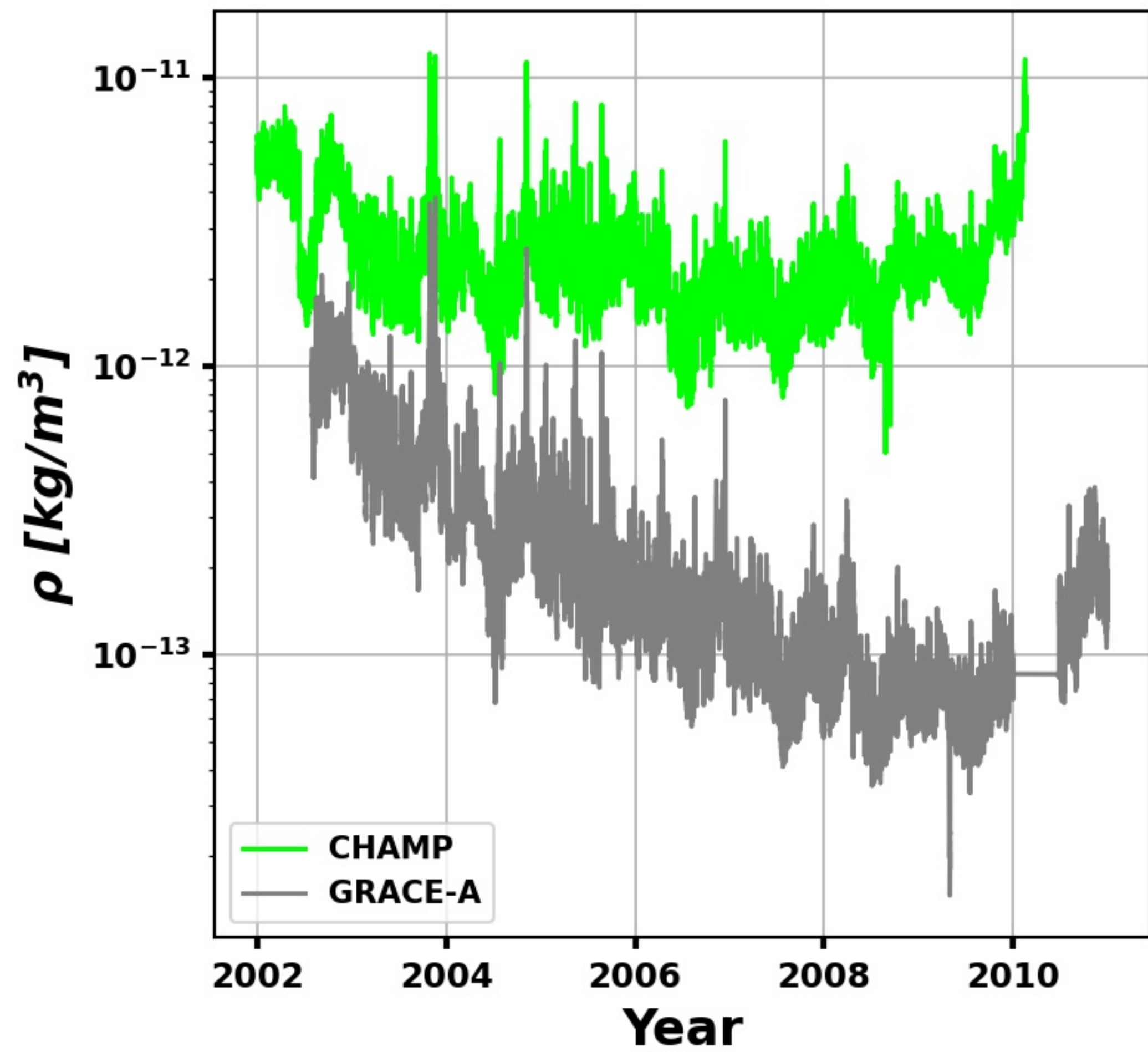
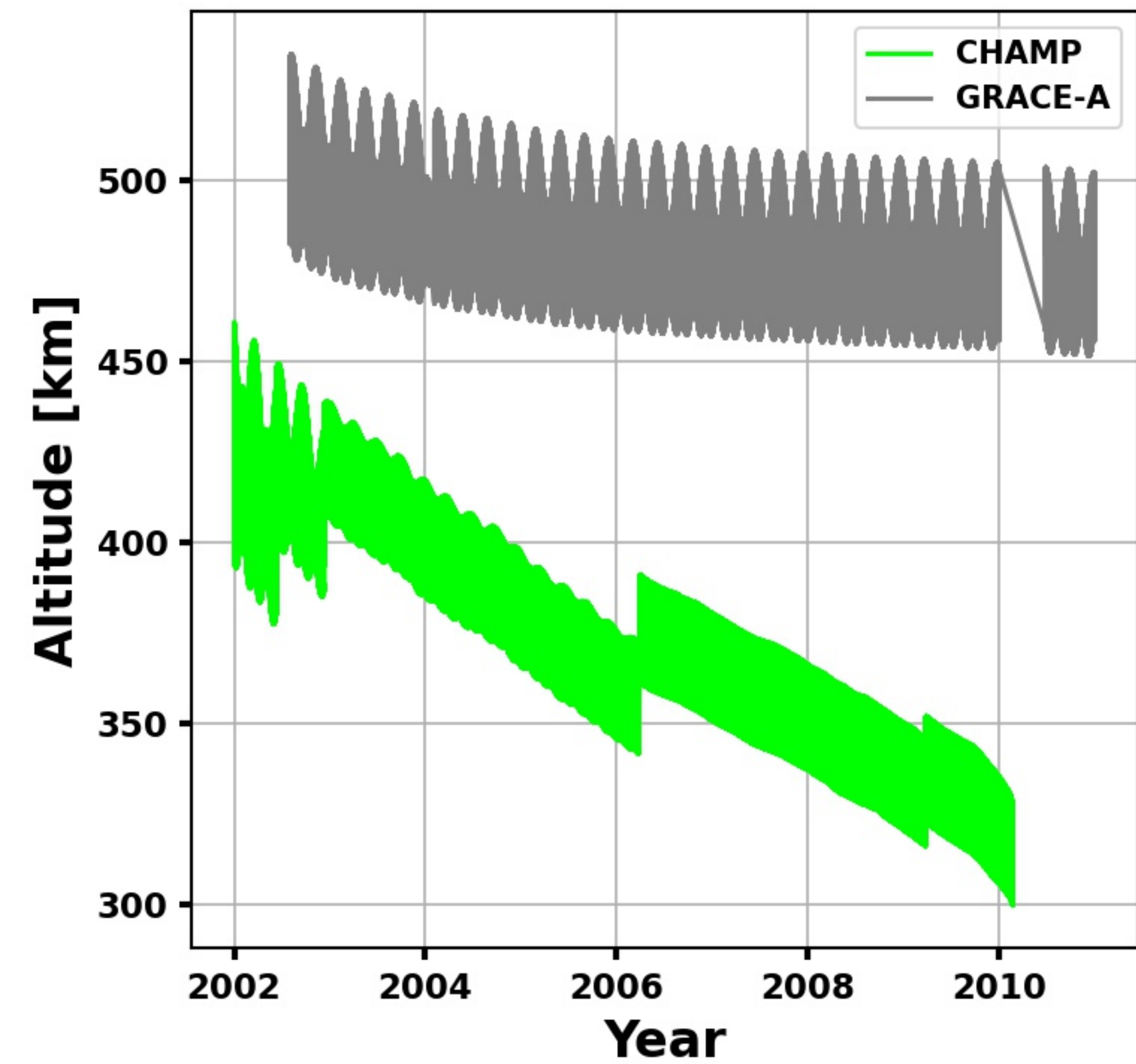


Figure 10.

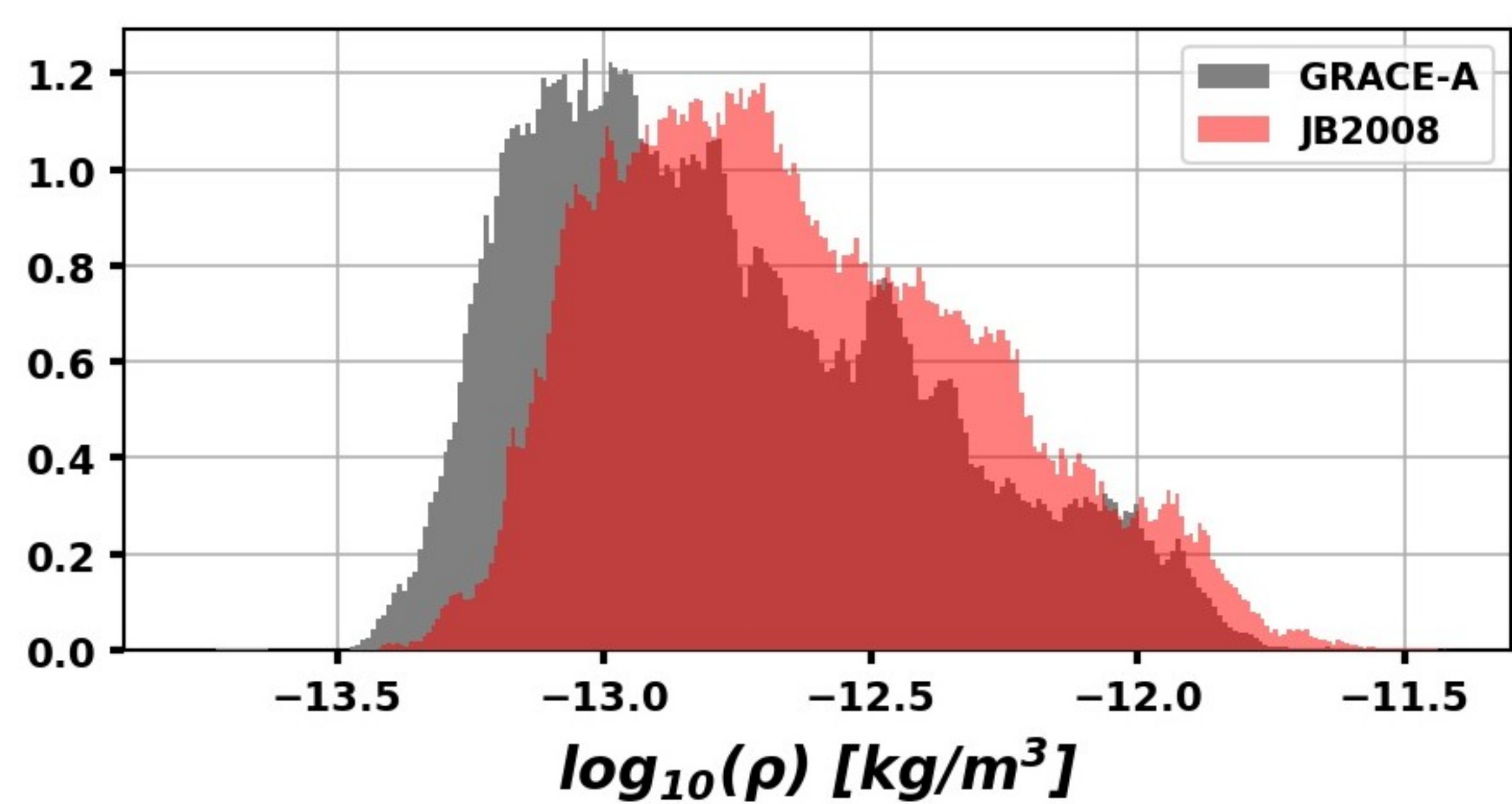
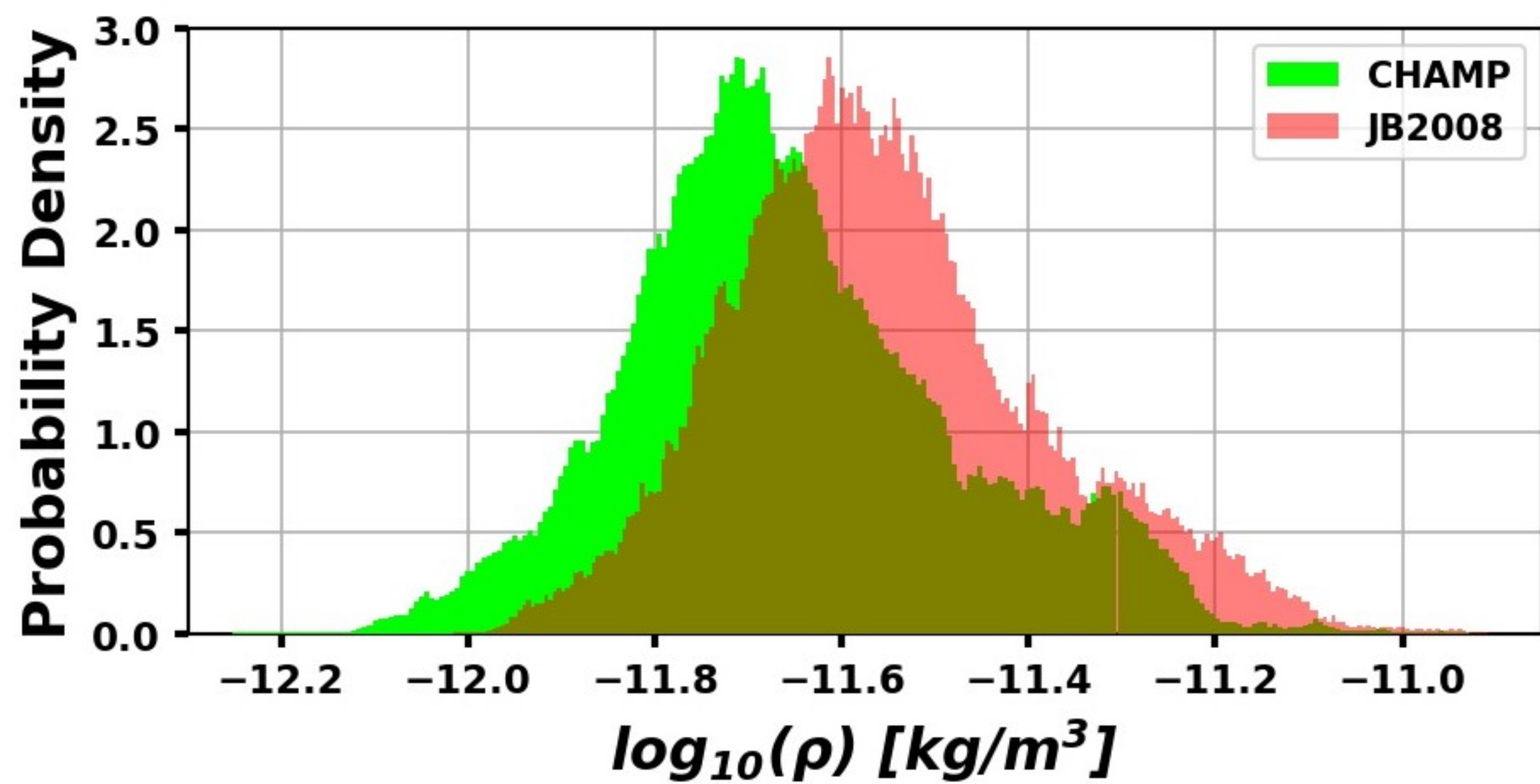
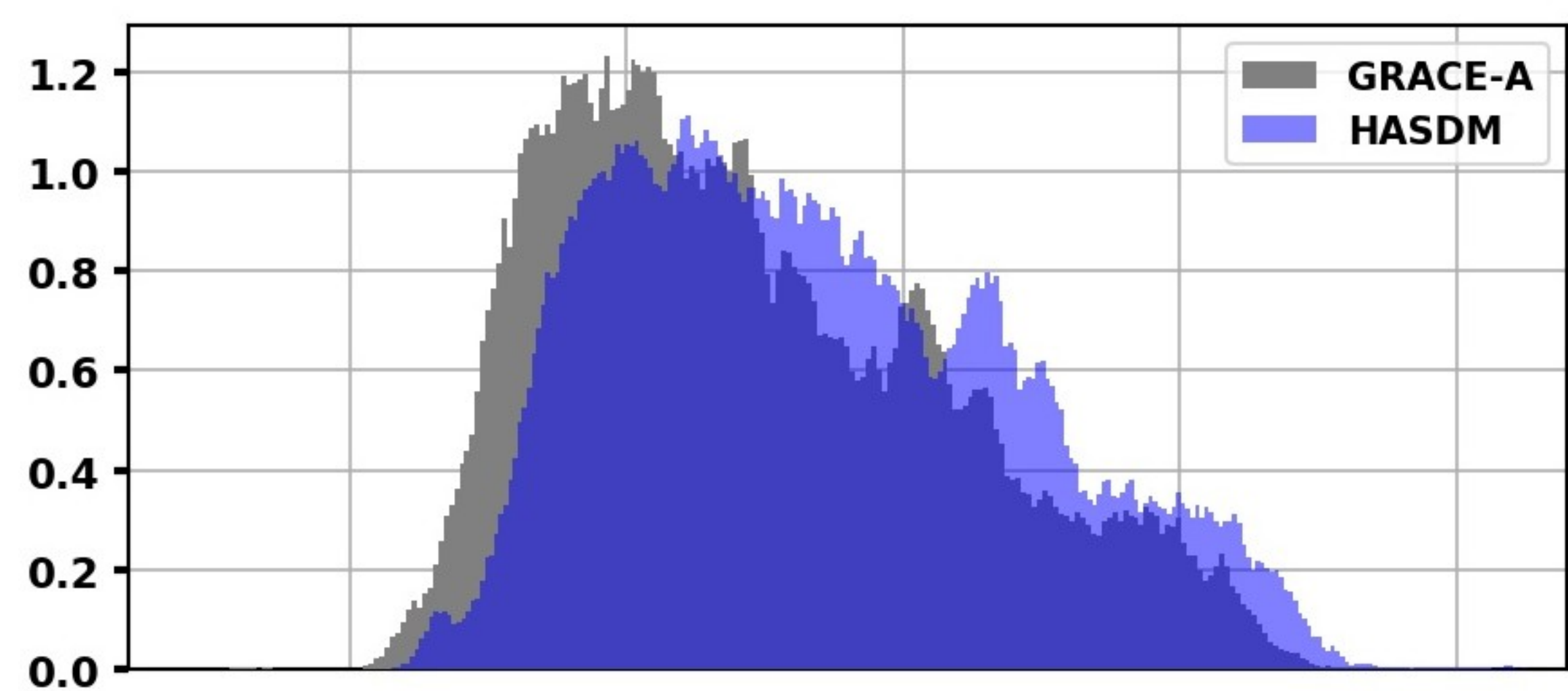
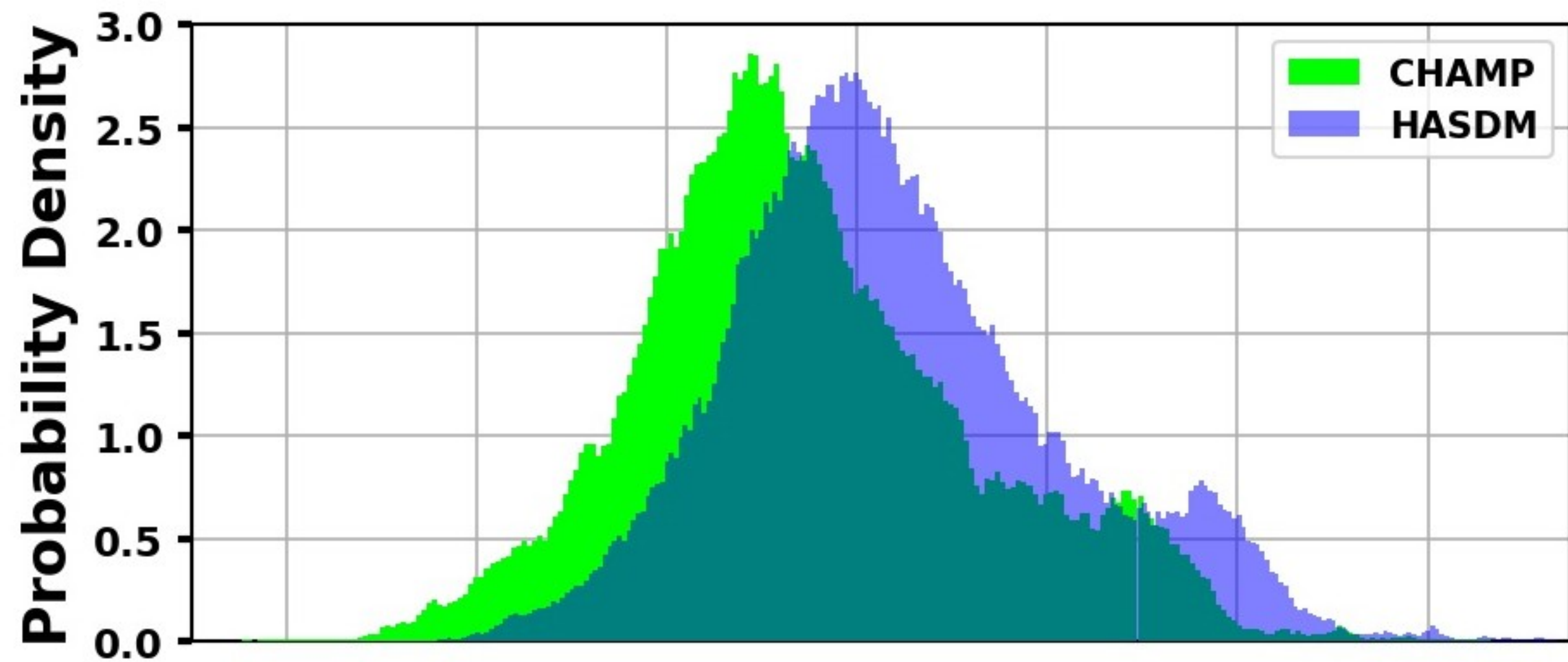


Figure 11.

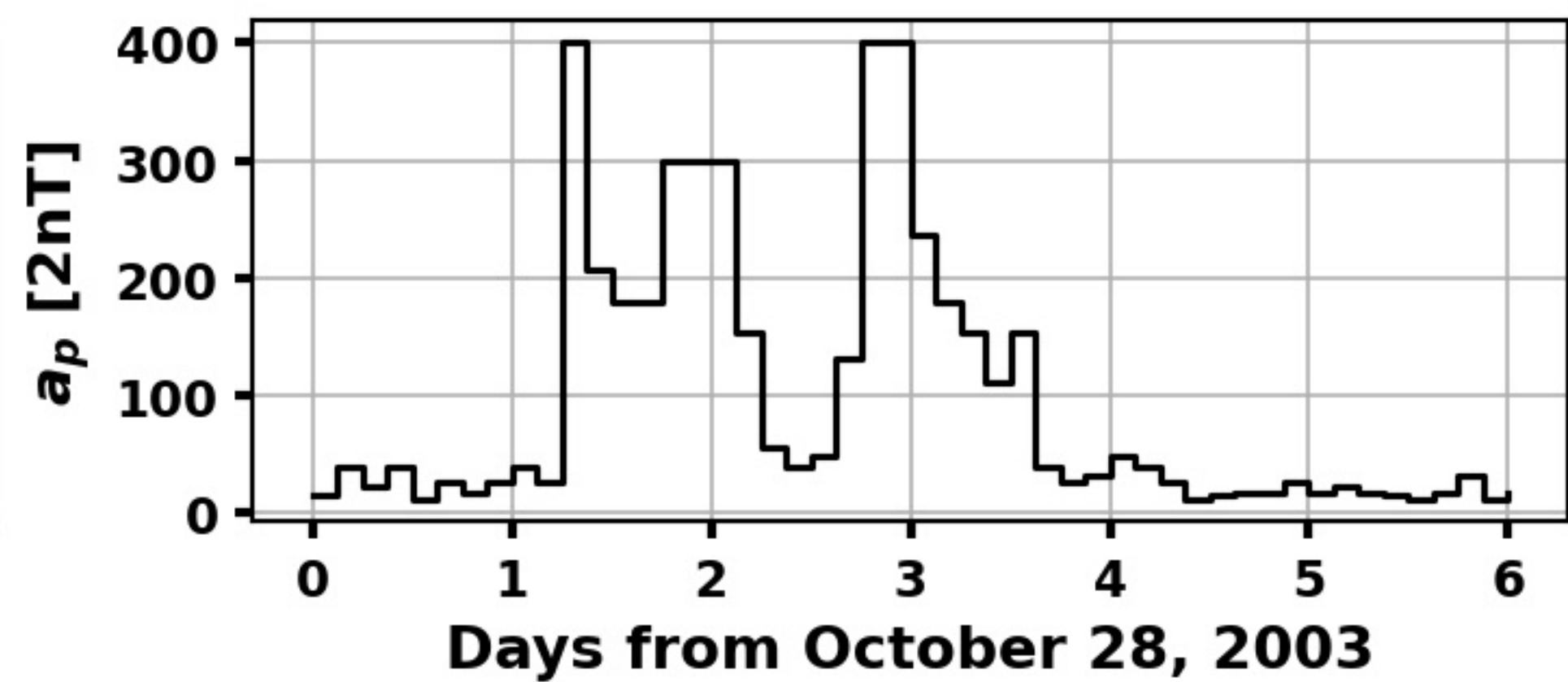
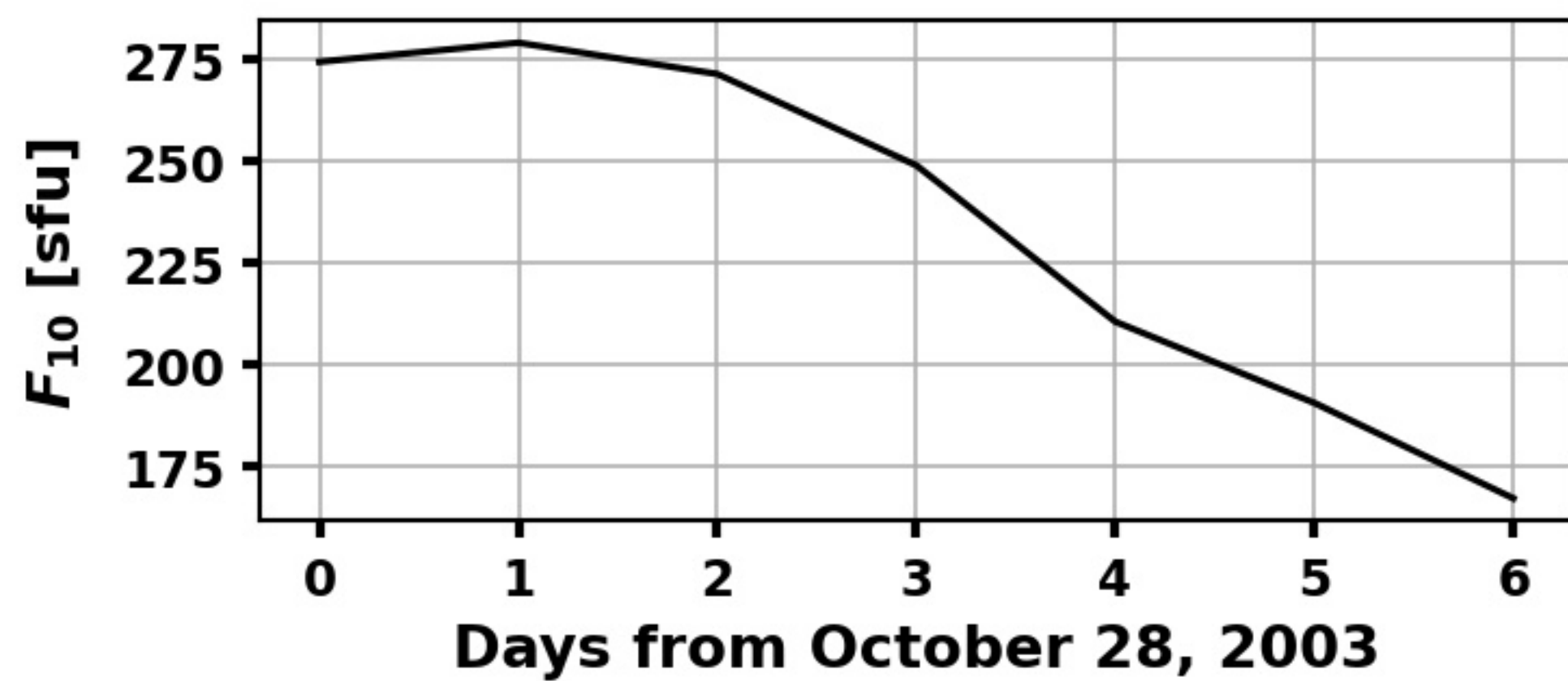
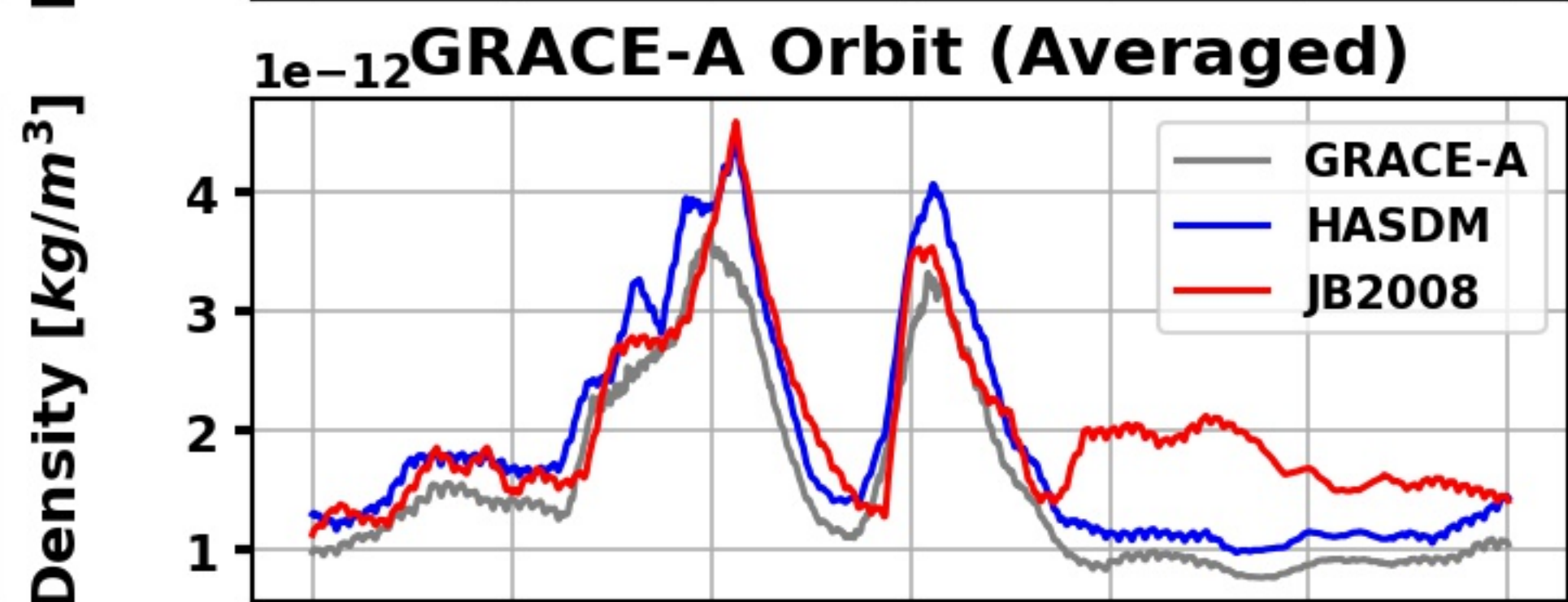
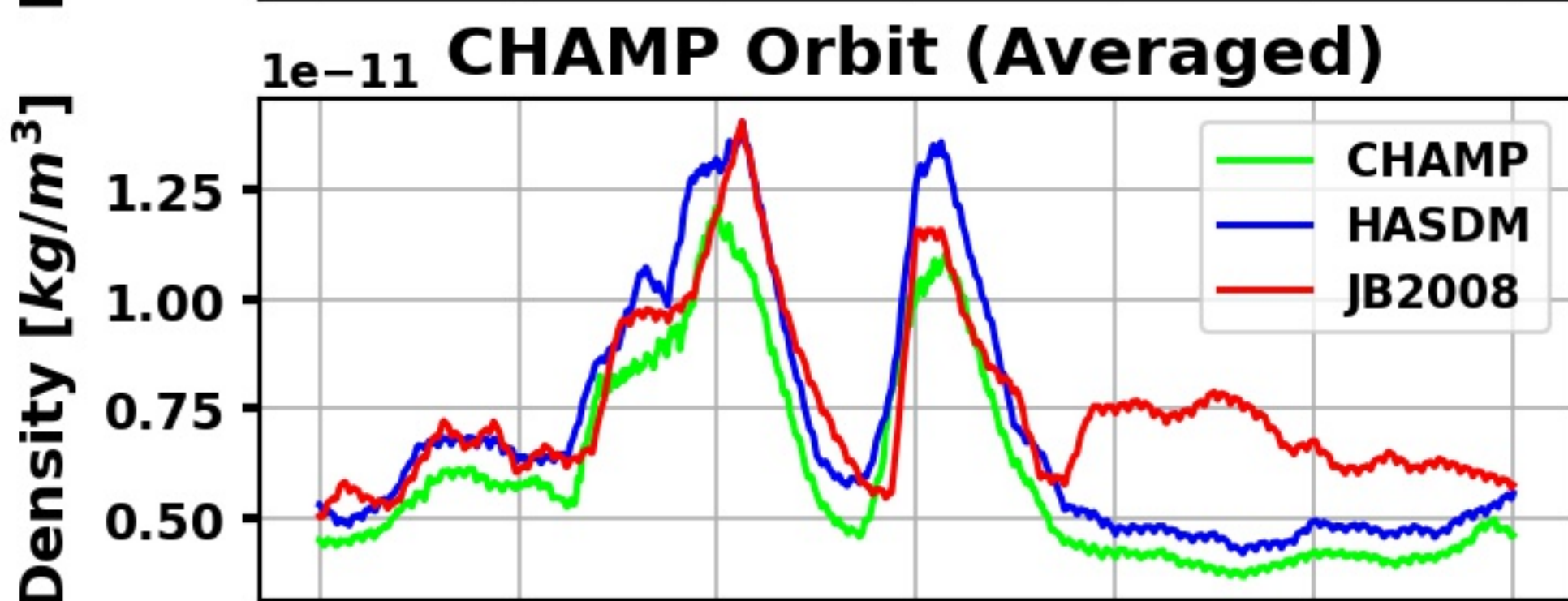
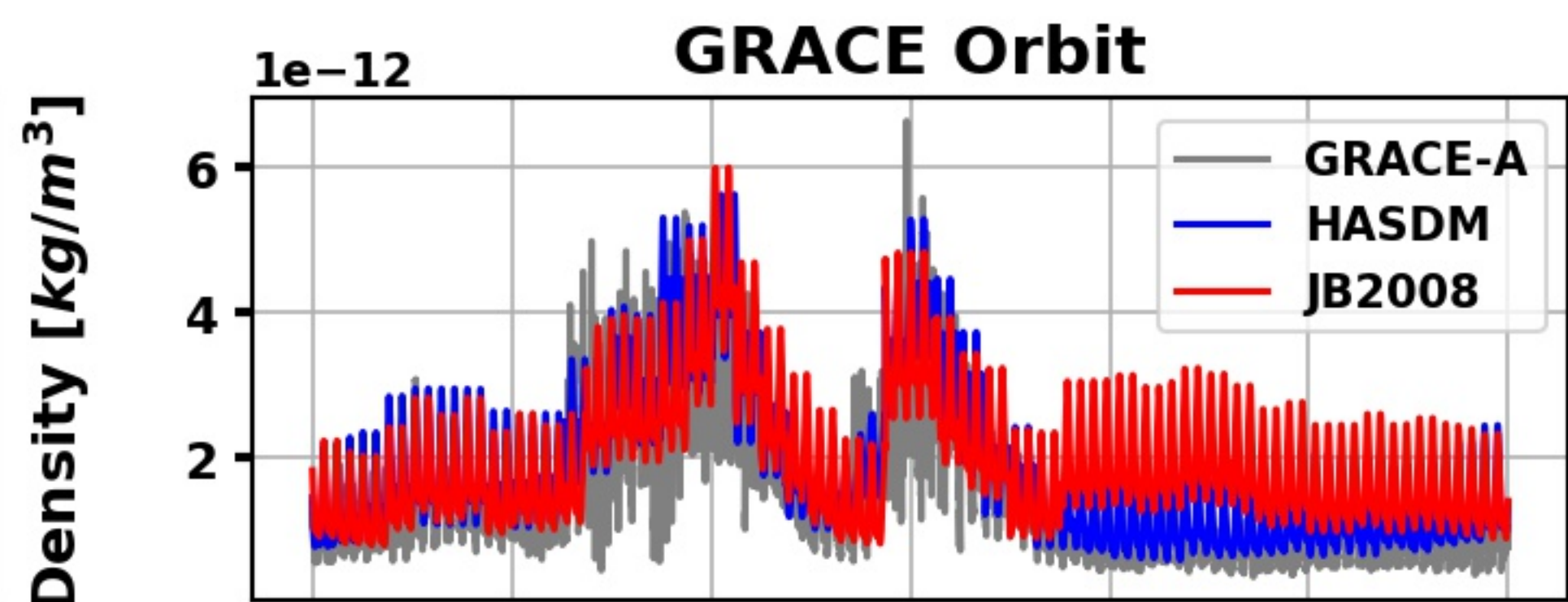
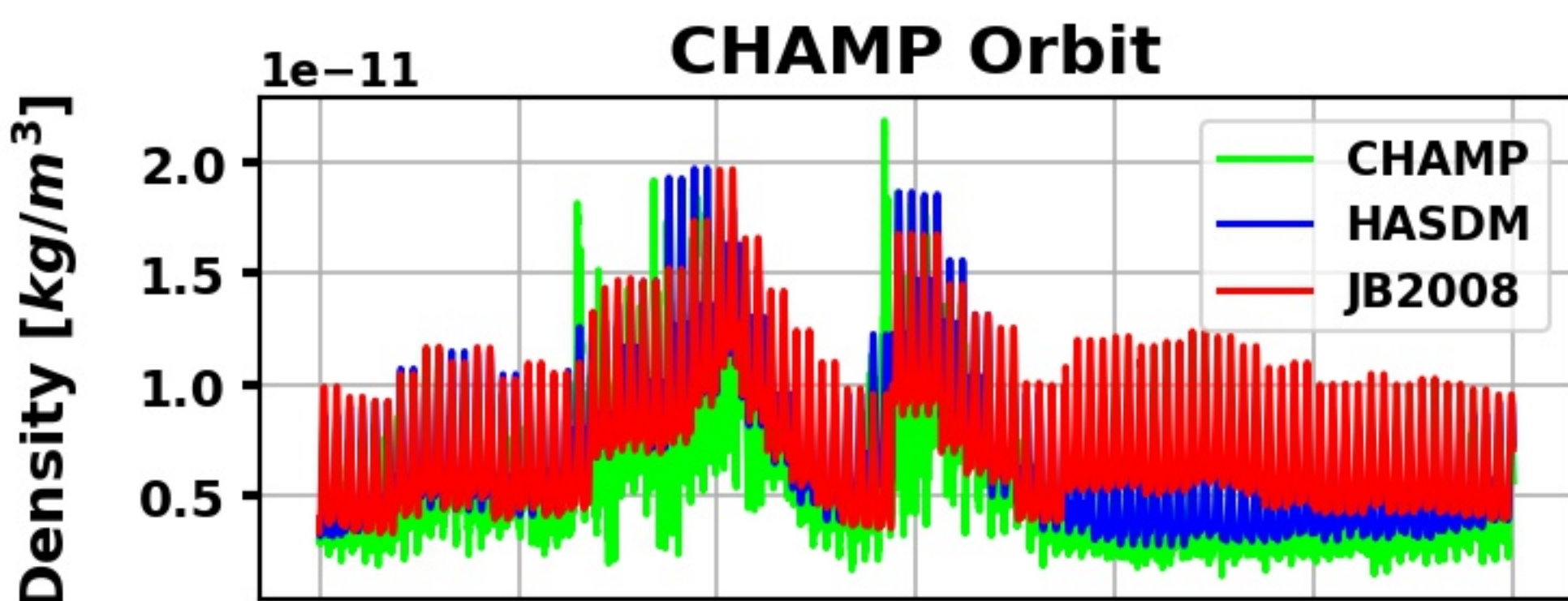


Figure 12.

